



Norwegian University of  
Science and Technology

# Effect of lanthanum on cobalt nickel catalysts for catalytic combustion of methane

**Najma Ali Abdullahi**

Chemical Engineering and Biotechnology

Submission date: June 2018

Supervisor: Jia Yang, IKP

Co-supervisor: Shirley Elisabeth Liland, IKP

Norwegian University of Science and Technology  
Department of Chemical Engineering



---

To Hooyo and Ayeeyo

To Aabo and Abdirazak

---

---

---

---

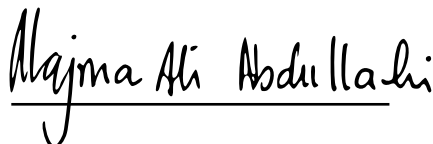
# Preface

This report is written for my Master's Thesis in the course TKP4900 Chemical Process Technology at the Department of Chemical Engineering, at the University of Science and Technology (NTNU). It is an extension of my Specialization Project in the course TKP4580 Catalysis and Petrochemistry. Also, it is the end of a five-year integrated master's degree program in the field called Chemical Engineering and Biotechnology. The project, including laboratory work, has been performed during the fall 2017 and spring 2018 at NTNU, with Associate Professor Jia Yang as the main supervisor and co-supervisor Ph.D. candidate Shirley Elisabeth Liland.

I would like to thank Associate Pr. Jia Yang for guidance and encouragements she has always given me. I would also like to thank the Ph.D. candidate, Shirley Elisabeth Liland for helping me with everything, from the laboratory work to the calculations. Finally, I would like to thank the engineers Karin, Harry, Estelle and Kristin (Department of Materials Science and Engineering) for the training and the help with the apparatus.

I hereby declare that this project is an independent work according to the exam regulations of the Norwegian University of Science and Technology (NTNU).

Trondheim June 12, 2018



*Najma Ali Abdullahi*

Najma Ali Abdullahi

---

# Abstract

The effect of lanthanum (La) on the catalytic behavior of nickel and cobalt catalysts derived from hydrotalcites in total combustion of methane was investigated. 12 wt. % Co (12Co), 12 wt. % Ni (12Ni) and 3.6 wt. %–8.4 wt. % Co (3.6Ni–8.4Co) were prepared by co-precipitation method followed by calcination and promoted further by 0.5–2 wt. % lanthanum using incipient wetness impregnation method. The final hydrotalcite-derived catalysts were characterized by x-ray diffraction (XRD), x-ray fluorescence (XRF), inductively coupled plasma-mass spectrometer (ICP-MS), temperature-programmed reduction (TPR),  $N_2$  adsorption and hydrogen chemisorption techniques. The XRD profiles confirmed the hydrotalcite structure of dried samples. The nitrogen adsorption demonstrated high surface area, 136–172  $m^2/g$  and small pore diameter of 10.4–13.2 nm. Hydrogen chemisorption presented slightly varied dispersion and metallic surface area.

The addition of La promoter to the catalysts showed slightly decreased dispersion, as well as BET surface area, except from 3.6Ni–8.4Co catalyst which its BET surface area was observed to increase with 0.6–5 %. On the other hand, the La promoter increased the interaction between the cobalt oxides and the hydrotalcite (HT) support, while for the nickel oxides, the opposite was observed.

The methane combustion over the nonpromoted and promoted catalysts was performed in a fixed-bed quartz reactor followed by gas chromatography (GC), mass spectrometry (MS) and ultraviolet-visible spectrometry (UV-Vis). The UV-Vis measurements were performed to study the oxidation states of the hydrotalcite-derived catalysts. This technique enabled to observe that oxidation state increased with temperature, where the oxidation state fraction was observed to decrease by La promotion in 12Ni catalyst.

The catalysts were mainly analyzed for methane conversion. Methane conversion showed to increase with the cobalt-contained catalysts and the temperature, where 3.6Ni–8.4Co catalyst was found to exhibit the highest activity on methane combustion among the catalysts. However, all the catalysts displayed decreasing methane conversion over time due to deactivation assigned to carbon formation on catalysts, as the TGA results showed. No significant changes were observed in the methane conversion with the addition of lanthanum, except from 12Ni–2La which showed lower methane conversion. Indeed, La promoter had two main effects on the catalysts. It blocked/covered parts of the nickel/cobalt active sites, at the same time it increased the remaining active sites. It also decreased the oxidation state fraction of the catalysts.

# Table of Contents

<b>Preface</b>	<b>i</b>
<b>Abstract</b>	<b>ii</b>
<b>Table of Contents</b>	<b>v</b>
<b>Abbreviations</b>	<b>vi</b>
<b>Symbols</b>	<b>vii</b>
<b>1 Introduction</b>	<b>1</b>
1.1 Background . . . . .	1
1.2 Objective . . . . .	2
1.3 Outline . . . . .	2
<b>2 Literature Review</b>	<b>3</b>
2.1 Catalytic combustion of methane . . . . .	3
2.2 Catalysts for catalytic combustion of methane . . . . .	4
2.2.1 Cobalt and nickel catalysts . . . . .	5
2.2.2 Bimetallic catalysts . . . . .	6
2.2.3 Role of promoters . . . . .	6
2.2.4 Hydrotalcite like-compounds . . . . .	7
2.3 Compact multichannel reformer . . . . .	8
<b>3 Basic Theory</b>	<b>11</b>
3.1 Catalyst synthesis . . . . .	11

---

3.1.1	Co-precipitation	11
3.1.2	Incipient wetness impregnation	12
3.1.3	Calcination	13
3.1.4	Reduction	13
3.2	Catalyst characterization	13
3.2.1	X-Ray Diffraction (XRD)	13
3.2.2	X-Ray Fluorescence (XRF)	14
3.2.3	Inductively Coupled Plasma Mass Spectrometer (ICP-MS)	14
3.2.4	Nitrogen adsorption	15
3.2.5	Temperatur Programmed Reduction (TPR)	16
3.2.6	Hydrogen chemisorption	17
3.2.7	Thermal Gravimetric Analysis (TGA)	18
3.2.8	Diffuse reflectance spectroscopy	18
3.3	Activity measurement	19
3.3.1	Gas Chromatography	19
3.3.2	Mass Spectrometry	20
3.3.3	Methane conversion	21
<b>4</b>	<b>Materials and methods</b>	<b>23</b>
4.1	Materials	23
4.2	Catalyst synthesis	23
4.2.1	Co-precipitation	24
4.2.2	Reduction and passivation	24
4.2.3	Incipient wetness impregnation	25
4.3	Catalyst characterization	25
4.3.1	X-Ray Diffraction (XRD)	25
4.3.2	X-Ray Fluorescence (XRF)	26
4.3.3	Inductively Coupled Plasma-Mass Spectrometer (ICP-MS)	26
4.3.4	Nitrogen adsorption	26
4.3.5	Temperature Programmed Reduction (TPR)	26
4.3.6	Hydrogen chemisorption	26
4.3.7	Thermal Gravimetric Analysis (TGA)	27
4.4	Catalytic activity test	27
<b>5</b>	<b>Results and discussion</b>	<b>31</b>
5.1	Catalyst characterization	31
5.1.1	X-Ray Diffraction (XRD)	31

---



---

5.1.2	X-Ray Fluorescence (XRF)	36
5.1.3	Inductively Coupled Plasma-Mass Spectrometer (ICP-MS)	37
5.1.4	Nitrogen adsorption	37
5.1.5	Temperature Programmed Reduction (TPR)	39
5.1.6	Hydrogen chemisorption	41
5.2	Catalytic activity results	42
5.2.1	UV-Vis evaluation of the catalysts	42
5.2.2	Methane conversion and catalyst stability	45
5.2.3	Deactivation of the catalysts	49
<b>6</b>	<b>Conclusion</b>	<b>53</b>
<b>7</b>	<b>Further research</b>	<b>55</b>
	<b>Bibliography</b>	<b>57</b>
	<b>Appendices</b>	<b>I</b>

---

# Abbreviations

BET	:	Brunauer-Emet-Teler
CPR	:	Catalytic plate reactor
GC	:	Gas Chromatography
HT	:	Hydrotalcite
HTlcs	:	Hydrotalcite like-compounds
ICP-MS	:	Inductively Coupled Plasma Mass Spectrometer
IUPAC	:	International Union of Pure and Applied Chemistry
MCC	:	Methane catalytic combustion
MCR	:	Methane compact reformer
MS	:	Mass Spectrometer
MSA	:	Metallic surface area
MSR	:	Methane steam reforming
Redox	:	Reduction-oxidation
TCD	:	Thermal Conductivity Detector
TGA	:	Thermal Gravimetric Analysis
TMIs	:	Transition metal ions
TPR	:	Temperature Programmed Reduction
UV-Vis	:	Ultraviolet Visible
XRD	:	X-ray diffraction
XRF	:	X-ray Fluorescence

# Symbols

$C_{CH_4}$	:	Concentration of $CH_4$ [ $mol/L$ ]
$C_{CO}$	:	Concentration of $CO$ [ $mol/L$ ]
$C_{CO_2}$	:	Concentration of $CO_2$ [ $mol/L$ ]
$d$	:	diameter
$d_{Co}$	:	Particle size of cobalt [ $nm$ ]
$d_{Ni}$	:	Particle size of nickel [ $nm$ ]
$D_M/D$	:	Metallic Dispersion [%]
$D_p$	:	Pore diameter [ $nm$ ]
$F_{CH_4}$	:	Molar flow of methane
$\Delta H_{298}^\circ$	:	Standard heat of reaction at 298 K [ $kJ/mol$ ]
$S_{BET}$	:	BET specific surface area [ $m^2/g$ ]
$N_{(s)M}$	:	Total Number of Metal atoms on the Surface
$N_{(T)M}$	:	Total Number of Metal atoms
$R$	:	Reflectance [%]
$V_p$	:	Pore volume [ $cm^3/g$ ]
$X_{CH_4}$	:	Methane conversion [%]

## TABLE OF CONTENTS

---

# Introduction

## 1.1 Background

Methane is a primary component in natural gas [25], which is a fossil fuel used for heating, cooking and transport fuel [38]. In 2014, 21.6 % of the world's electricity was produced from natural gas, which means natural gas is increasingly playing an important role in the world's energy [20]. According to the data from International Association of Natural Gas Vehicles (IANGV), there will be up to 65 million Natural Gas Vehicles on the road by 2020 [8], confirming the importance of Natural Gas for the future.

It is well-known that methane is used for the production of synthesis gases ( $H_2$ ,  $CO_2$ , CO ...) in chemical industries. Synthesis gases are feedstocks for many valuable chemical productions such as ammonia-, methanol- and Fischer-Tropsch synthesis and can be made through methane Steam Reforming process (MSR).[43] A very high temperature is necessary to get complete conversion of methane during the MSR process. However, this is crucial for the industries because of energy costs. This heat requirement can be met by coupling steam reforming with catalytic methane combustion through compact multi-channel reformer [62]. Another problem with fuel combustion due to high temperature is formation of nitrogen oxides ( $NO_x$ ).

Even though methane is an important energy source hydrocarbon, it is also a major constituent in the green house gases. According to the International Energy Agency [25], methane is 25 times more powerful than  $CO_2$  as a green house gas. It is also a major by-product of many industrial processes [12]. It is, therefore, necessary to convert unburnt methane to minimize both the energy inefficiency and green house effects. Catalytic combustion of methane can cover these problems, as well as the emission abatement.

The main advantages of catalytic combustion of natural gas/methane are that reactions can be carried out over a wide range of fuel/air ratios and at lower temperature ranges [66].

However, catalytic combustion process brings up new challenges, namely the catalyst stability problems. Deactivation of the catalyst can involve sintering or poisoning [32]. Nickel and cobalt supported on hydrotalcite-like compounds (HTLcs) have been extensively studied for catalytic combustion of methane and showed good performances [8, 10]. Hydrotalcite materials have shown to be resistance to sintering [36]. According to the literature, the hydrotalcite properties can be enhanced even better by addition of small amounts of rare earth metals, such as lanthanum (La) [36, 44]. This Master's project focuses on hydrotalcite-derived nickel and cobalt catalysts promoted with lanthanum on total combustion of methane. Indeed, nickel and cobalt catalysts' performances will be evaluated.

## 1.2 Objective

The main objectives of this Master's project are

1. To study how lanthanum will affect the physical and chemical properties of the HT supported nickel and cobalt catalysts.
2. To evaluate if lanthanum addition enhances the methane conversion.

## 1.3 Outline

The outline of this Master's thesis is as following:

Chapter 1 is the introduction and presents the main objective of this thesis.

Chapter 2 is a literature review, focusing on the investigations that are relevant for the thesis.

Chapter 3 is the theoretical background about catalyst synthesizing and characterization methods that are important for this project.

Chapter 4 presents all needed information for reproduction of the experimental work.

Chapter 5 presents the results and discusses them.

Chapter 6 concludes the thesis and chapter 7 suggests improvements for further research.

# Literature Review

## 2.1 Catalytic combustion of methane

Methane combustion has been studied for the production of heat and removal of unburnt fuel [8, 28]. The overall equation for the total oxidation of methane or natural gas is given below [5, 32]:

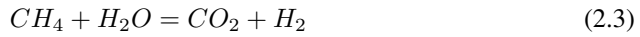


Equation 2.1 is a simplification of many free radical chain reaction, which can only occur at 1600 °C or above [32]. In this condition undesired reactions can be formed, such as nitrogen oxides ( $NO_x$ ) (if  $N_2$  is not separated from air)[32], this can be avoided by catalytic combustion, which is reaction of organic compounds such as hydrocarbons by using solid catalysts [28] and will allow to control reaction conditions and temperature [20, 66]. Indeed, this leads to using energy more efficiently and minimizing pollutant emissions [59].

Catalytic combustion of methane is generally categorized into three classes according to the temperature zones of the combustion systems; low-temperature combustion, which is operated below 300 °C, intermediate-temperature combustion, which is operated at 300-800 °C and high-temperature combustion which is operated above 800 °C. [28]

Catalytic combustion of methane can produce carbon monoxide and hydrogen gases as by-products, depending on the air to methane ratio, through partial oxidation (2.2),

steam reforming (2.3) and the water gas shift (2.4) reactions [32]:



However, methane is very difficult to oxidize at low temperature, since it has the strongest C-H bond among the hydrocarbons, which means its conversion needs highly active catalysts which are stable at very high temperatures [32, 33, 61]. Complete oxidation of methane is strongly influenced by two factors, namely the oxygen to methane ratio and catalyst activity. Having the correct oxygen to methane ratio increases the selectivity and avoids the by-product; *CO*. A highly active catalyst depends upon the support, its resistance to poisons, preparation method, etc.[32]

## 2.2 Catalysts for catalytic combustion of methane

Noble metal catalysts have shown to be best efficient catalysts for catalytic methane combustion [9, 32]. Methane oxidation is favored when the noble metals are supported, which makes the noble metal catalysts to disperse over a greater surface area. The most widely used noble metal catalysts are palladium (Pd) and platinum (Pt) due to their high activity. However, these catalysts are very expensive and are not stable at high temperatures [10, 53] and therefore replaced with non-precious transition metals [54].

Transition metals have multiple valance states, which means they can easily form redox cycle between oxidation states. Transition metal-based catalysis can therefore release and restore oxygen at the same time. [8] Transition metal-based catalysis has some disadvantages such as lower catalytic activity and higher light-off temperatures [12, 63]. However, the transition metal-based catalysts can have better activities and stability than noble metals with proper ingredients and preparation methods [8, 63]. One of these methods is described in section 2.2.4.

McCarthy et al [51] reported the activity of supported single metal oxides for methane oxidation as following:  $Co_3O_4 > CuO > NiO > Mn_2O_3 > Cr_2O_3$ . There have been many studies on transition metal composite oxides derived from hydrotalcites, which have shown to be noble combustion catalysts, due to having good catalytic activity, stability and high dispersion of active sites [10, 27].



### 2.2.1 Cobalt and nickel catalysts

Cobalt-based catalysts are found to be one of the best candidates for catalytic combustion of methane [9, 41, 59]. Moreover, cobalt oxides have been proven to exhibit weak oxygen bond strength and high turnover frequency for redox reactions [33], due to the low bulk heat of formation of cobalt oxide. Thus, the ease of removal of oxygen from cobalt oxide can give higher conversion [55].

Among the cobalt-based catalysts,  $Co_3O_4$  has shown to be a very active component for catalytic combustion of methane [8, 59]. However,  $Co_3O_4$ -catalysts suffer from sintering at temperatures as low as 500 °C and easy evaporation at temperatures from 997 °C [41]. This has drastic effect on its catalytic performance and decreases it [8]. The sintering problem can be avoided or minimized by using supports, because supports lead to stabilization of the cobalt ions [8].

T.-c. Xiao et al. investigated cobalt-based catalysts supported on four different metal oxide metals ( $ZrO_2$ ,  $MgO$ ,  $TiO_2$  and  $Al_2O_3$ ) and their catalytic performance in methane oxidation [59]. In this study, it was observed  $ZrO_2$  supported cobalt to have the highest activity at lowest temperature, as well as the lowest light-off temperature, due to support's special interaction with the active component.  $MgO$  supported cobalt showed lower activity than  $ZrO_2$ , as well as higher temperature for completely converted methane, but has better catalytic performance than  $TiO_2$  support. The  $Al_2O_3$  supported cobalt gave the lowest activity with very high light-off temperature. [59] Y. Gou et al. [19] observed that mixed cobalt-nickel oxides give higher catalytic performance than pure  $NiO$  and  $Co_3O_4$  for carbon monoxide oxidation. Indeed, an appropriate mixture  $NiO$  and  $Co_3O_4$  can obtain high activity for methane combustion, since mixed oxides can have desirable intrinsic property [33].

Nickel is also one of the mostly researched transition metals for the catalytic combustion of methane, due to its low-cost and long-proven performances [44]. Dissanayake et al. [16] observed that  $NiO/Al_2O_3$  catalyzes the complete oxidation of  $CH_4$ , while metallic nickel (Ni) supported on alumina is the active site for partial oxidation of methane [31]. F. Liu et al. [34] found  $NiO$  catalyst to have higher catalytic activity for methane combustion than the perovskite catalyst  $LaCoO_3$ , due to its larger capability for oxygen adsorption. Indeed, activation of oxygen plays an important role in methane combustion for the surface kinetics controlled region [34].

### 2.2.2 Bimetallic catalysts

Bimetallic catalysts systems have got important role in the energy and environmental applications, because of having better electronic and chemical properties than their own metals. This may show enhanced performances, but depends on the metal compositions, preparation methods and metal morphostructure. [15] There are many catalytic processes with bimetallic catalysts such as Fischer-Tropsch synthesis, *CO* hydrogenation, selective hydrogenations and oxidative reactions [14].

A bimetallic catalyst system consists of a main component,  $M_1$  and an added component  $M_2$  which interact with each other. This interaction between the two metals can affect the surface of the metals and is divided into geometric and electronic effects. The geometric effects are originated from the surface of  $M_1$  atoms, which decrease due to the dilution of the  $M_2$  components and forming an ensemble result. This can affect the reaction activity, since the most of the reactions depend on the surface atoms. The electronic effect occurs due to the difference in the electronic affinity between  $M_1$  and  $M_2$  and may influence significantly the activity and selectivity. [14]

T. Miyake and T. Asakawa [42] report that metal leaching that occur in the oxidation reactions can be reduced by bimetallic catalyst systems. J. Zhang et al. [64] observed that the bimetallic of Ni-Co catalyst decreased the coke formation due to synergetic effects, high metal dispersion and strong metal-support interactions.

### 2.2.3 Role of promoters

In catalysis, promoters are used as additives to enhance the active sites of the catalysts [11]. Promoters are observed to alternate acid-base property of the catalysts, to improve the dispersion of the active species and to increase the interaction between the active species and the support [65].

A range of different promoters have been studied for the catalysts in methane/hydrocarbon combustion. J. Chen et al. [8] reports that addition of rare-earth metals such as La, Zr, Ce and other metals has been proven to stabilize both the support and the active phase of *Pd/Al<sub>2</sub>O<sub>3</sub>*. A. F Lucredio et al [35] studied cobalt and nickel catalysts derived from hydrotalcite promoted with Ce and La in catalytic partial oxidation of methane. This study has shown the additives (Ce, La) to increase the CO selectivity and decrease the carbon formation, because the additives favored the adsorption and decomposition of oxygen on the catalysts [35, 36].

S. Natesakhawat et al. [44] had also studied the steam reforming of propane over *Ni/Al<sub>2</sub>O<sub>3</sub>* catalysts promoted with lanthanide elements (La, Ce and Yb).

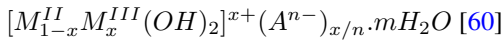
The cerium (Ce) promoted  $Ni/Al_2O_3$  showed highest performance by increasing both  $C_3H_8$  conversion and  $H_2$  yield, due to higher reducibility of nickel species and larger surface area of nickel. Hence, the addition of La on Ni-based catalysts increases the dispersion, surface area and strengthen the interaction between the Ni active sites and the support [36, 44, 65], but depending upon the nature of the support and preparation method.

On the other hand, addition of La on Co-based catalysts reported to decrease BET surface area and lower reducibility [21, 22, 35]. Indeed, "the addition of small amounts of rare earth oxides, which have the basic properties, to the structure of hydrotalcite, can change the hydrotalcites' characteristics after thermal treatment by the increase the of the hydrotalcites' basicity" [35, 36].

### 2.2.4 Hydrotalcite like-compounds

Hydrotalcite belongs to anionic clays group. The name indicates that it looks like talc or talcum (hydrated magnesium silicate). It is also hydroxycarbonate of magnesium and aluminum with chemical formula as  $Mg_6Al_2(OH)_6CO_3 \cdot 4H_2O$ . Hydrotalcite has exchangeable anions and is simple and inexpensive to prepare in the laboratory. A method that gives compositions which are optimal for hydrotalcite like-compounds is co-precipitation. This method is especially good for non-noble metal-based catalysts. Indeed, hydrotalcite like-compounds obtained by co-precipitation method have high surface area, basic properties and metal crystals that are thermally stable. [7]

Generally, hydrotalcite like-compounds (HTlcs) have chemical formula as:



, where  $M^{III}$  is cationic ions with charge +3,  $M^{II}$  is cationic ions with charge +2 and  $A^{n-}$  is compensatory for anions (organic/inorganic). This chemical formula for HTlcs shows the atomic contents of the HTlcs-structure. The literature has shown that  $M^{II}$  can be  $Mg^{2+}$ ,  $Co^{2+}$  and  $Ni^{2+}$ , where  $M^{III}$  is cations like  $Al^{3+}$ . For the most cases  $A^{n-} = CO_3^{2-}$ . x has values [0.1, 0.5], where x-values between 0.2 and 0.33 give the best HTlcs-structure according to literature [7]. To get efficient hydrotalcite like-compounds, the following conditions must be fulfilled [25]:

$$0.2 \leq \frac{M^{III}}{M^{II} + M^{III}} \leq 0.4$$

$$\frac{1}{n} \leq \frac{A^{n-}}{M^{III}} \leq 1$$

Calcining hydrotalcite like-compounds at high temperature results in transformation of hydrotalcite into small crystals. These small crystals have a mixture of interactive metal oxides, which allow high specific area, good dispersing and thermal stability [46].

During reduction of HT-supported catalysts, metal oxides go to metals. This means the calcined products are in forms such as  $CoO$ ,  $NiO/MgO/Al_2O_3$  and go to  $Co$ ,  $Ni/MgO/Al_2O_3$  after reduction [46].

## 2.3 Compact multichannel reformer

In multifunctional reactors, there are two or more processes, where mass, heat and momentum transport are functioning, and reactions occur integrated or independently [2, 62]. The main function can be to couple highly endothermic reactions with highly exothermic reactions to meet the heat demands [62] or to reach other improvements such as yield and productivity [2]. Multifunctional reactors exist in many large-scale industrial processes such as Autothermal Reforming Process [2], hydrocarbon cracking and dehydrogenation [62].

The exothermic reaction as heat exchange and the endothermic reaction can be combined in three ways; *in situ*, *chronologically segregated* and *spatially segregated* heat generations. Reactants for the exothermic and endothermic reactions are run paralleled in the *in-situ* heat generation, for instance, the industrially applied secondary methane reforming process with ammonia process [62].

The *chronologically segregated* heat generation is cycled in such a way that the heat from the exothermic reaction is stored in fixed bed, which will be consumed by the endothermic reaction, so the fixed bed is cooled down. There have been different studies on chronologically segregated heat exchange between steam reforming and catalytic methane combustion [62]. The chronologically segregated and *in-situ* heat generations have brought up new challenges. The *in-situ* needs bifunctional catalysts that will assist the endothermic and exothermic reactions in the same temperature domain, which may limit the conversion. For the chronologically segregated heat generation, hot spots may occur, causing damage to the catalyst and the reactor materials [62].

In the *spatially segregated* heat generation, the endothermic reactions receives heat from the exothermic reactions indirectly [62], something has shown spatially segregation to be the main compact multichannel reformer over the two others. Figure 2.1 is showing a spatially segregation of heat generation, where the endothermic reaction (methane steam reforming) and the exothermic reaction (methane catalytic combustion) are combined through solid wall of two-layered catalysts.

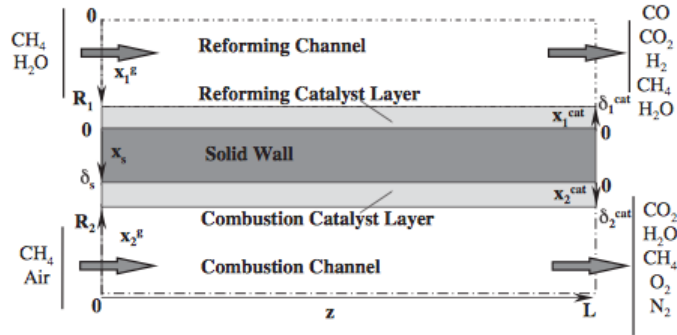


**Figure 2.1:** Methane steam reforming coupled with methane catalytic combustion in a catalytic plate reactor (CPR) developed by M. Zanfir [62].

Abdullah Irankhah and his colleagues [26] investigated methane steam reforming (MSR) integrated with methane catalytic combustion (MCC) in a methane compact reformer (MCR) to produce hydrogen as illustrated in Figure 2.2. Indeed, the multichannel compact reformer has three simultaneous processes: catalytic combustion, heat recovery and the methane steam reforming (MSR) in the multichannel system, where the MSR and MCC are integrated in a plate or monolithic reactor with many catalyst-coated channels [26]. Although compact multichannel reformer can reduce energetic cost and generate enough hydrogen, its drawback can be heat loss due to temperature drop, catalyst deactivation and possible combustor explosion due to high temperature [26].

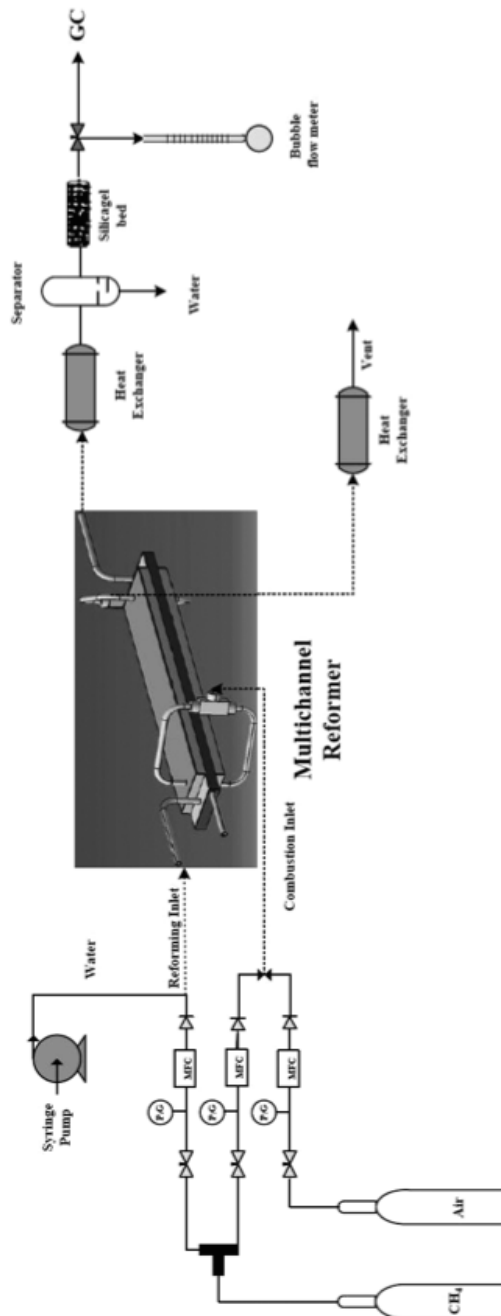


**Figure 2.2:** Methane steam reforming (MSR) in a methane compact reformer developed by Abdullah Irankhah [26]. The multichannel reformer consists of two sections: (1) the MSR section and (2) the combustor section consisting of two multichannel plates.

## Basic Theory

### 3.1 Catalyst synthesis

#### 3.1.1 Co-precipitation

In catalysis, co-precipitation is used to synthesize catalysts based on more than one component to precipitate them simultaneously. Co-precipitation is obtained by adding precipitating agent, hence  $NaOH$  and  $Na_2CO_3$  with the solution of precursor salts. [11] The precursor salts are consisting of the catalyst active material and the support [11, 13]. To remove water and  $CO_2$  the hydroxy salt precipitates are dried. The co-precipitation method gives homogeneous distribution of components with definite stoichiometry, which can also result to achievement of the active catalyst. Calcination and/or reduction are used as final steps to create small, well distributed and dispersed crystallites from the mixtures of different compounds. [17] [Figure 3.1](#) is an illustration of how precipitated catalysts can be obtained from co-preparation method.

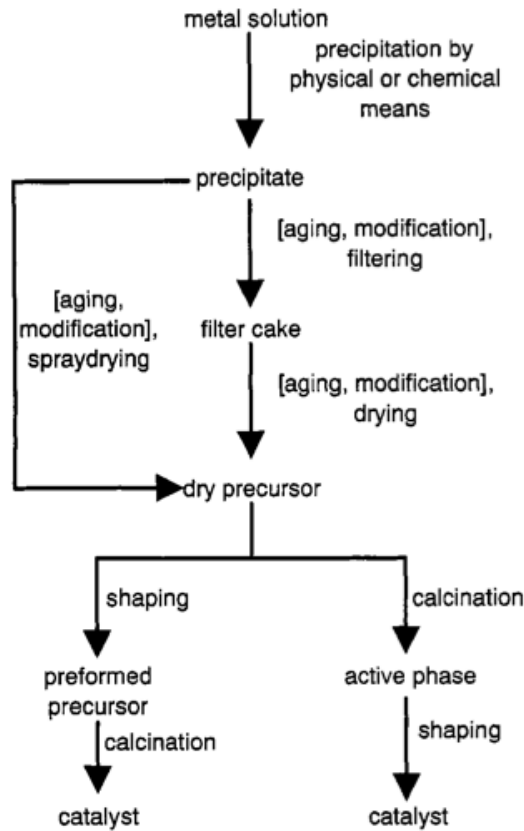


**Figure 3.1:** Preparation scheme for precipitated catalysts. Optional preparation steps are indicated by square brackets [17].

### 3.1.2 Incipient wetness impregnation

Impregnation means to introduce an active element onto the support, where the dissolved catalyst precursor is interacting with the surface of the support [13, 17]. Impregnation is often obtained by filling the pores of the support with dissolved metal precursors, where the volume solution is equal to the pore volume [3]. The solvent is then removed by drying. This method is called incipient wetness impregnation and is used to disperse active components over supports. After the promoted precursors have been dried, the catalyst precursors are calcined to remove the remaining water and nitrates from the salt solution. [11]



### 3.1.3 Calcination

Calcination is a thermal process where solid materials are heated to high temperatures in air or oxygen atmosphere [58]. The process is used to decompose, do phase transition or remove volatile fractions, which converts the precursors to chemically strong-bonded catalyst products [17, 58]. Calcination is an important step in catalyst preparation and is executed carefully to avoid undesired products such as sintering. During the calcination process, metal oxides are formed.[17]

### 3.1.4 Reduction

Removal of oxygen from the catalysts occurs during the reduction step, where hydrogen gas is added to the metal oxide catalyst at an elevated temperature [11]. Reduction generates a highly porous material with high mechanical strength and active component up to 96-98 % [17]. Indeed, reduction is executed  $H_2$ -stream diluted with inert gas such as argon to avoid sintering of the metal [58].

## 3.2 Catalyst characterization

### 3.2.1 X-Ray Diffraction (XRD)

X-ray diffraction (XRD) is a powerful technique used to determine crystal structures of compounds and indication of particle size [11]. Determining crystalline structures of compounds gives information about the substance, such as bond length and bond angle [48]. The below figure is showing the fundamental theory for XRD:

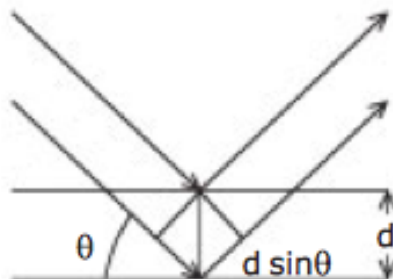


**Figure 3.2:** Bragg diffraction, where the incoming arrows are representing the x-ray beam applied on the sample and the outgoing ones are showing the diffracted beams [11].

A well-known equation used for determinations of crystalline structures is Bragg's equation shown below [11, 37]:

$$n\lambda = 2d\sin\theta \quad (3.1)$$

, where  $d$  is the space between planes,  $\theta$  is the diffraction angle adjacent to the atomic planes,  $\lambda$  is the wavelength and  $n$  is an integer number, also known as the order of reflection [11]. Consider that an x-ray beam is sent to a powder. This radiation transmits, emits and scatters. Diffraction occurs when there is interference of the scattered waves. The constructive interference depends on the wavelength of the radiation ( $\lambda$ ) and the atomic spacing, in terms of  $d$  and  $\theta$ . The Bragg relation (Equation 3.1) gives the lattice spacing ( $d$ ) by measuring  $2\theta$ , which is characteristic for every compound [11].

XRD does not give information about amount of compositions exactly, but the composition basis determines the intensity of different diffraction, which is donated by  $n$  in equation 3.1 [29]. Indeed, the x-ray diffraction technique gives unique structure information about particles when they are sufficiently large [11, 29, 37]. However, XRD is very insufficient when the amount of a compound is very small compared to other substances in the sample, which means the small amounts will go undetected, the same happens if the particles are also too amorphous [11].

### 3.2.2 X-Ray Fluorescence (XRF)

X-ray fluorescence (XRF) is a qualitative, quantitative and non-destructive spectroscopic analyzing method, which reveals the atomic compositions of a certain sample. XRF-method can analyze both solid and liquid samples. This method is best for samples with elements from Na to U. This technique is based on the use of an x-ray beam causing excitation of electrons and ionization. First, the electrons in the inner shells excite to outer shells. Then the electron from outer levels transit to the vacant positions of the exited electrons, and some energy is given off, known as x-ray fluorescence. The energy of the emitted electron (fluorescence) is characteristic for the element, and is proportional to the atomic mass and the concentration of the element. The XRF-results are very dependent on the preparation stages, such as pellet preparations. [39]

### 3.2.3 Inductively Coupled Plasma Mass Spectrometer (ICP-MS)

Inductively coupled plasma mass spectrometry (ICP-MS) is an analytical technique used for elemental determination. It has been one of the best analytical techniques since the 1980s, due to its ability to analyze most elements at low concentrations, having high degree of selectivity, precision and accuracy. [50] ICP-MS is based on high temperature plasma,

which converts the atoms presented in the samples to ions. The ions are separated and detected by a mass spectrometer (MS) [50].

### 3.2.4 Nitrogen adsorption

The surface area of porous materials with surface area greater than  $1\text{-}2\text{ m}^2/\text{g}$  can be measured by nitrogen adsorption. Liquid nitrogen can be adsorbed on the solid surface (catalyst). The number of  $N_2$ -molecules adsorbed at the monolayer coverage can calculate the internal surface area, because each adsorbed  $N_2$ -molecule has surface area that is comparable with the cross-sectional area of  $N_2$ -gas.

A well-known equation that is used to determine the volume of the adsorbed nitrogen as function of relative pressure is the BET-equation (developed by the professors Brunauer, Emet and Teler ). [49]:

$$\frac{P}{V(P_0-P)} = \frac{1}{V_m C} + \frac{(C-1)P}{V_m C P_0} \quad (3.2)$$

$P$  : Partial pressure of  $N_2$

$P_0$  : The saturation pressure at a given temperature

$V$  : The volume adsorbed at partial pressure of  $N_2$

$V_m$  : The volume adsorbed at the monolayer coverage

$C$  : Constant

The assumptions which must be fulfilled for application of the above equation is found in [17]. The BET-plot gives differently-shaped graphs, which can indicate the porosity size of a sample and this is shown in the left figure in Figure 3.3. According to IUPAC, type I isotherms indicate that the sample is microporous ( $d \leq 2\text{ nm}$ ) and has small external surface area such as molecular sieve zeolites [17]. The type II isotherms are characteristic for macroporous solids ( $d \geq 50\text{ nm}$ ) and represents combination of multilayer and monolayer (there is an adsorption at some points; B and no adsorption at other points). Type IV isotherms are characteristic for mesoporous solids ( $2\text{ nm} \leq d \leq 50\text{ nm}$ ). This type has a hysteresis loop in addition to type II isotherm shape, which is explaining the capillary condensation taking place in the mesoporous pores. Type III and type V isotherms are not common, while type VI isotherms are characteristic for argon/krypton graphitised on carbon blacks [17, 49].

IUPAC has also classified the adsorption-desorption hysteresis as following [17, 49]:

H1 which is typical for mesoporous samples with narrow distribution of adsorption. H2 is characteristic for carbon activated samples with complex network of pore structure.

H3 and H4 do not have well-defined mesoporous structure, hence difficult to derive either the pore size distribution or the total pore volume distribution from these isotherms. H3 is given by plate-like materials such as clays. [17, 49]

The adsorption-desorption hysteresis loops are shown in the right figure in figure [Figure 3.3](#).

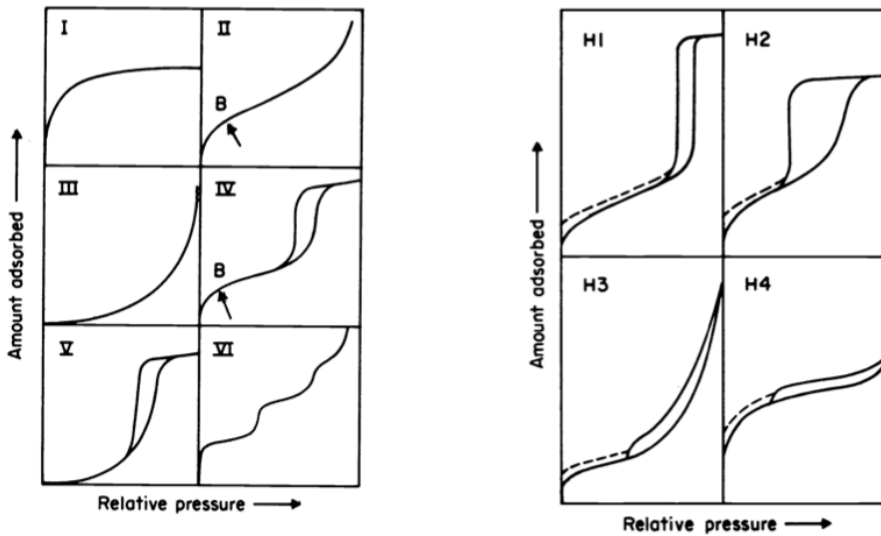
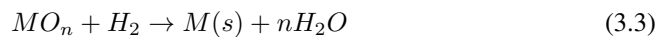


**Figure 3.3:** The types of physisorption isotherms and hysteresis loops [49].

### 3.2.5 Temperatur Programmed Reduction (TPR)

Temperature programmed reduction (TPR) measures the temperature needed for a complete reduction of the catalysts. The measurement takes place in a reactor, controlled by a processor heating the catalyst inside the reactor linearly, with a controlled hydrogen flow to the reactor. A thermal conductivity detector (TCD) records the hydrogen consumption. [11] During the reduction of metal oxides by  $H_2$ , the following chemical reaction takes place for metal oxides added with hydrogen gas [45]:



, where  $MO_n$  is a metal oxide and  $M(s)$  is the formed metal. Whether the catalyst is reduced or not is determined thermodynamically.  $\Delta G$  in [Equation 3.4](#) must be negative, in order to get the reduction fulfilled. [45]:

$$\Delta G = \Delta G^0 + nRT \ln \frac{P_{H_2O}}{P_{H_2}} \quad (3.4)$$

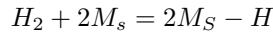
, where  $\Delta G$  is the Gibbs free energy at temperature  $T$ ,  $\Delta G^0$  is standard Gibbs free energy,  $P$  is the partial pressure and  $n$  is the stoichiometric coefficient. Indeed, the second term in Equation 3.4 is always negative, because water is removed during the TPR experiment.  $\Delta G^0$  is also negative for the most metal oxides, such as nickel and cobalt. Hence, the TPR is thermodynamically feasible [45].

### 3.2.6 Hydrogen chemisorption

Metal dispersion ( $D_M$ ) is defined as the ratio between the total number of metal atoms on the surface ( $N_{(s)M}$ ) and the total number of metal atoms present ( $N_{(T)M}$ ), which can be expressed mathematically as [3]:

$$D_M = \frac{N_{(s)M}}{N_{(T)M}} \quad (3.5)$$

$H_2$ -chemisorption is a widely used characterization technique to determine the metal dispersion of catalysts. It is assumed that hydrogen adsorbs dissociatively on metals as [30]:



, where  $M_s$  stands for the metal surface atom. Stoichiometrically, one hydrogen atom occupies per metal surface. The main feature is that the sample is pre-treated. The pretreatment consists of removal of water, reduction of the catalyst and evacuation. The reactor contacts with a known amount of hydrogen gas at room temperature, where the repeated hydrogen pulses get chemisorbed on the catalyst. The quantity of adsorbed hydrogen gas is determined by measuring the pressure after a while until reaching the equilibrium pressure. The metal dispersion of catalyst is calculated from Langmuir isotherm adsorption of hydrogen, where volume adsorbed is plotted against the pressure [17]. The metal dispersion is calculated from the following equation [30]:

$$D = \frac{v_m n}{22414m} / \frac{wt}{100M} \quad (3.6)$$

, where  $v_m$  is in  $cm^3$  (STP),  $n$  is the chemisorption stoichiometry,  $m$  is the sample mass (g),  $wt$  (%) is the metal loading and  $M$  is the atomic mass of the metal. The higher the dispersion is, the larger availability of metal atoms for chemisorption of gas phases and subsequent catalytic reaction [6].

The particle size can be determined from the dispersion and indeed, the nickel particle size ( $d_{Ni}$ ) and cobalt particle size ( $d_{Co}$ ) are respectively calculated as the following [46]:

$$d_{Ni} = \frac{101}{D} [nm] \quad (3.7)$$

$$d_{Co} = \frac{96}{D} [nm] \quad (3.8)$$

, where the main assumption is that the particles have spherical forms. The average particle size of the mixture of cobalt and nickel ( $d_{Ni-Co}$ ) is also calculated as the following [46]:

$$d_{Ni-Co} = \left( \frac{101}{D_{Ni}} x(\%Ni/100) + \frac{96}{D_{Co}} x(\%Co/100) \right) [nm] \quad (3.9)$$

### 3.2.7 Thermal Gravimetric Analysis (TGA)

Thermal Gravimetric Analysis (TGA) is a thermal analytical technique which measures the mass loss of samples as a function of temperature. The temperature is increased linearly over time while the mass changes are recorded due to oxidative, reduced or inert atmospheres. [11] TGA is always monitored with a DSC (Differential Scanning Calorimetry) which keeps sample and reference at the same temperature. Sometimes, MS (Mass Spectrometer) is monitored to the TGA to identify the gaseous compositions in the sample.

### 3.2.8 Diffuse reflectance spectroscopy

In diffuse reflectance spectroscopy, both d-d and charge transfer transitions can be examined to get information about oxidation states and coordination conditions of transition metal oxides [56, 57]. This spectroscopic method is based on the reflection of light on a sample, where the light is in the ultraviolet (UV) and visible (Vis) light region. The applied UV-Vis light on the sample can either be reflected, absorbed or transmitted. For example to evaluate the nickel and cobalt states during the reduction and combustion steps, the diffuse reflectance spectroscopy can be applied.

Kubelka and Munk developed an equation which correlates the absorption and reflection of the light from transmittance measurements [57]:

$$F(R_{\infty}) = \frac{(1 - R_{\infty})^2}{2R_{\infty}} = \frac{K}{S} \quad (3.10)$$

, where  $R_{\infty}$  is the diffuse reflectance of the sample,  $K$  and  $S$  are the absorption and the scattering coefficients respectively. The Kubelka-Munk function ( $F(R_{\infty})$ ) is valid under these conditions [57]:

1. diffuse monochromatic irradiation of the powder sample
2. isotropic light scattering
3. an infinite layer thickness
4. a low concentration of TMIs
5. a uniform distribution of TMIs
6. absence of fluorescence

According to Robert and Bert [57],  $\frac{K}{S}$  often have values between 0 and 0.3. For values  $\frac{K}{S}$  greater than 0.3  $F(R_\infty)$  decreases. Large values of  $F(R_\infty)$  means high absorption of the UV-Vis light by the powder.

## 3.3 Activity measurement

### 3.3.1 Gas Chromatography

A gas chromatography (GC) is powerful instrument to analyze mixtures of components in industries and academia. The technique is based on a stationary phase and a mobile phase. The stationary phase is a bed with a large surface, in which the mobile phase is percolating through. Usually, the mobile phase, also known as a carrier, is an inert gas such as helium. The stationary phase is a high boiling liquid coated on the inside of a capillary column. The vaporized mixture is carried by the mobile phase through the column, while a program controls the temperature in the column. The components are separated according to their volatility at specific temperature. The separated components leave the column and are detected, where the most volatile component leaves the column first. [40] The output signals from the detector are known as chromatograms and explains the interactions between the components and the stationary phase. This is expressed by the equilibrium constant,  $K_C$ , which tells the tendency of a component to be attracted to the stationary phase [40]:

$$K_C = \frac{A_S}{A_M} \quad (3.11)$$

, where  $A_S$  is the concentration of the component in the stationary phase and  $A_M$  is the concentration of the component in the mobile phase. Indeed, the equilibrium constant,  $K_C$  is proportional to the solubility of the component in the stationary phase, which gives rise to chromatograms peaks.

### 3.3.2 Mass Spectrometry

Mass spectrometry (MS) is an analytic technique, which analyzes samples by converting atoms to ions and separating them according to their mass to charge ratio ( $m/z$ ). The MS principle is based on four different stages: a vaporized sample is bombarded with an electron beams, creating only positively charged electron, known as the ionization stage. The ionized sample is then accelerated in an electric field and is sent to magnetic field which will deflect the ions according to mass to charge ratio. The ions with small charges and large mass will be deflected less. The deflected ions are detected electrically. A vacuum pump is needed in order that the ions produced in the ionization chamber have a free run through the machine without hitting air molecules [50]. Figure 3.4 is illustrating the different parts in a mass spectrometry. In this project, a thermostar MS (ThermoStar TM GSD 301 T) was used, where the MS is connected to a Q500 thermogravimetric analyzer (TA instrument), which allows to analyze qualitatively all of the gases in the TA instrument.

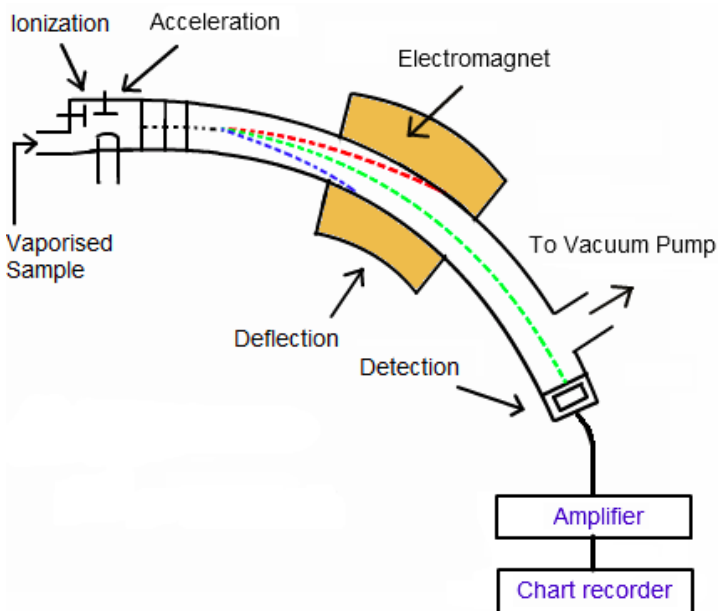


**Figure 3.4:** Schematic configuration of mass spectrometer stages [1].



### 3.3.3 Methane conversion

The methane conversion is defined as:

$$X_{CH_4} = \frac{F_{CH_4,in} - F_{CH_4,out}}{F_{CH_4,in}} \quad (3.12)$$

The methane oxidation products were analyzed by GC instrument Agilent 6890N equipped with FID and TCD detectors, where the methane conversion was calculated from integrated peaks areas under the gas chromatograms. The following equation was used to determine the concentration of the  $i$  components,  $C_i$ :

$$C_i = A_i * RF_i \quad (3.13)$$

, where  $A_i$  is the integrated area of component  $i$  from the GC and  $RF_i$  is its response factor. When the concentration of the product components was determined, the methane conversion,  $X_{CH_4}$  was calculated as the following, based on equation 3.12:

$$X_{CH_4} = \frac{C_{CO} + C_{CO_2}}{C_{CO} + C_{CO_2} + C_{CH_4}} * 100 \quad (3.14)$$

The derivation of 3.14 from 3.12 is found in appendix A.2.1.



# Materials and methods

This section details the experimental work performed for the catalyst synthesis, characterization and activity test.

## 4.1 Materials

Materials used to synthesize hydrotalcite-derived nickel cobalt catalysts in this thesis are given in [Table 4.1](#).

**Table 4.1:** Percentage of nickel and cobalt in the prepared catalysts.

Materials	Chemical formula	Purity [%]	Manufacturer
Nickle nitrate hexahydrate	$Ni(NO_3)_2 \cdot 6H_2O$	>99.999	Sigma-Aldrich
Cobalt nitrate hexahydrate	$Co(NO_3)_2 \cdot 6H_2O$	> 99	Acros Organics
Lanthanum nitrate hydrate	$La(NO_3)_3 \cdot xH_2O$	> 99	Sigma-Aldrich
Magnesium nitrate hexahydrate	$Mg(NO_3)_2 \cdot 6H_2O$	> 99	Sigma-Aldrich
Aluminum nitrate nonahydrate	$Al(NO_3)_3 \cdot 9H_2O$	> 99	Sigma-Aldrich
Sodium hydroxide	$NaOH$	> 98	Merck
Sodium carbonate	$Na_2CO_3$	100	VWR Chemicals

## 4.2 Catalyst synthesis

Three different hydrotalcite-derived catalysts were prepared by the co-precipitation method. The metal loading was constant at 12 wt.% as shown in [Table 4.2](#). For catalyst preparation calculations, see appendix [A.1.1](#).

**Table 4.2:** Percentage of nickel and cobalt in the prepared catalysts.

Catalyst	Total metal loading [wt.%]	Nickel [wt.%]	Cobalt [wt.%]
12Ni	12	12	0
12Co	12	0	12
3.6Ni-8.4Co	12	3.6	8.4

The weight ratio between nickel and cobalt in 3.6Ni-8.4Co catalyst is fixed to be  $3/7 = 0.43$ .

### 4.2.1 Co-precipitation

12 wt.% Ni, 12 wt.% Co and 3.6 wt.% Ni–8.4 wt.% Co were prepared from hydrotalcite-like precursors by co-precipitation method.

12 wt.% metal loading nickel (Ni) was synthesized as following:

The cation precursors, consisting of 7.96 g  $Ni(NO_3)_2 \cdot 6H_2O$ , 50.77 g

$Mg(NO_3)_2 \cdot 6H_2O$  and 28.20 g  $Al(NO_3)_3 \cdot 9H_2O$  were dissolved into 400 mL of distilled water in a three-neck bottom flask with stirrer and condenser.

The anion precursors, consisting of 24.08 g  $NaOH$  and 5.99 g  $Na_2CO_3$  were dissolved into 400 mL of distilled water in a beaker. The anion mixture was then fed to the three-neck bottom flask (with cation precursors), droplet by droplet for two hours (h). After the cation and anion precursors were well dissolved, the pH was measured to be around 9 by adding droplets of  $HNO_3$ . After that, the solution was kept under stirring at 80 °C for 16 h. Then the precipitation was cooled down for a while, washed with distilled water and filtered until the filtration water-waste got pH to be 7. The obtained product was dried for 10 h at 70 °C and then calcined for 6 h at 600 °C with heating rate of 5 °C/min, see [Figure B.1](#) for the some of the obtained products. The prepared catalysts were sieved between 75  $\mu m$  and 150  $\mu m$ , see the picture in [Figure B.2](#). The amount of the raw materials used in the other catalysts is given in [Table A.5](#).

### 4.2.2 Reduction and passivation

Before the catalysts were impregnated with lanthanum (La), every catalyst was reduced and passivated, in a fixed bed quartz reactor fitted with thermocouple measuring the temperature inside. Around 3.5 grams of catalyst was reduced with 75 mL/min He and 75 mL/min  $H_2$  at 670 °C for 16 h at a heating rate of 2 °C/min. After reduction and  $H_2$  gas was shut down for 2 h, the catalysts were passivated with 100 mL/min 1 %  $O_2/Ar$  for 2 h at room temperature.

### 4.2.3 Incipient wetness impregnation

The reduced and passivated catalysts were impregnated with 0.5 wt.%, 1 wt.% and 2 wt.% lanthanum (La) by incipient wetness impregnation method. 0.0158 g (0.5 wt.% La), 0.0317 g (1 wt.% La) and 0.0634 g (2 wt.% La) lanthanum(III) nitrate hydrate ( $La(NO_3)_3 \cdot xH_2O$ ) were dissolved in distilled water amounted as their own pore volume determined by the nitrogen adsorption. The mixtures were then mixed with 0.995 g, 0.99 g and 0.98 g catalysts respectively. To understand how these numbers were determined, check appendix A.1.2. The promoted catalysts were then dried and calcined with the same conditions as in section 4.2.1. Table 4.3 gives an overview of the nominal amount of lanthanum (La) in the catalysts.

**Table 4.3:** Percentage of lanthanum (La) in the promoted catalysts.

Catalyst	Total metal loading [wt.%]	Nickel [wt.%]	Cobalt [wt.%]	Lanthanum [wt.%]
12Ni-0.5La	12	12	0	0.5
12Ni-1La	12	12	0	1
12Ni-2La	12	12	0	2
12Co-0.5La	12	0	12	0.5
12Co-1La	12	0	12	1
12Co-2La	12	0	12	2
3.6Ni-8.4Co-0.5La	12	3.6	8.4	0.5
3.6Ni-8.4Co-1La	12	3.6	8.4	1
3.6Ni-8.4Co-2La	12	3.6	8.4	2

## 4.3 Catalyst characterization

The following sections, 4.3.1–4.3.7 describe detailed the characterization methods performed on the hydrotalcite-derived catalysts.

### 4.3.1 X-Ray Diffraction (XRD)

X-ray diffraction was done on the catalyst powders by using Routine Powder Diffractometer (DaVinci1) at the Department of Materials Science and Engineering, NTNU. The fine samples were made as flat as possible on the same height as the sample holder edges.

The wavelength was  $1.54.10^{-10}$  m. Every sample powder was analyzed at  $10^\circ - 80^\circ$  with step size of  $0.3^\circ$  for 2 h.

### 4.3.2 X-Ray Fluorescence (XRF)

To find the compositions of the synthesized catalysts, around 0.36 g calcined sample (particle size  $\leq 75 \mu\text{m}$ ) was mixed homogeneously with 2.7 g boric acid (binder) and turned into pellet. Then the pellet was analyzed by Rigaku SuperMini200 spectrometer, XRF.

### 4.3.3 Inductively Coupled Plasma-Mass Spectrometer (ICP-MS)

For elemental analyzes, 10 mg calcined sample was solved in a 1 mL  $\text{HNO}_3$  (65 % concentrated) and mixed well in an ultrasonic cleaner. The well-mixed samples were then diluted into 100 mL de-ionized water. The solution was analyzed by ICP-MS trippel quad Agilent 8800 at the Department of Chemistry at NTNU.

### 4.3.4 Nitrogen adsorption

The Micromeritics Tristar II 3020 Surface Area and Porosity Analyzer was used to determine the surface area, pore volume and average pore diameter from nitrogen adsorption measurements at liquid  $\text{N}_2$  temperature. Prior to vacuum, 50-100 mg calcined samples were overnight in VacPrep 061 Degasser unit at 200 °C. The specific surface area of the samples was determined by the BET-method, while the pore volume and pore diameter were calculated by the BJH-model.

### 4.3.5 Temperature Programmed Reduction (TPR)

100 mg calcined sample was placed in a U-shaped quartz reactor between wads of quartz wool and connected to the thermometer measurement. First, the temperature was increased from 0 to 300 °C to remove water and impurities. Then it was cooled down to the room temperature and TPR-analyzing was started. 7 %  $\text{H}_2/\text{Ar}$  was flowed into the reactor and the temperature was increased to 900 °C with heating rate of 10 °C /min. For every catalyst, the hydrogen consumption was collected by a thermal conductivity detector (TCD). The hydrogen reduction was performed on Altamira BenchCat Hybrid instrument.

### 4.3.6 Hydrogen chemisorption

The amounts of chemisorbed hydrogen on the hydrotalcite catalysts were measured using the Micromeritics ASAP 2020 instrument. 100-200 mg calcined samples was placed between quartz wool wads in a U-shaped reactor and connected to the thermometer measurement. To degass the sample, it was under vacuum for at least 2 hours. Then the reactor temperature was increased to 670 °C with heating rate of 10 °C /min, where the sample

was reduced *in situ* at 670 °C for 16 h. After the reduction the sample was cooled down to 40 °C to collect the isotherm adsorption for the metal dispersion. The catalyst and hydrogen gas stoichiometric ratio was assumed to be 1, meaning that one H atom is adsorbed on the metal. It was also assumed that neither La or the support contributed to chemisorption.

### 4.3.7 Thermal Gravimetric Analysis (TGA)

Quantitative analysis of water content in lanthanum(III) nitrate hydrate ( $La(NO_3)_3 \cdot xH_2O$ ) was performed by thermal gravimetric analysis (TGA) on Netzsch STA 449C instrument, to calculate the amount of lanthanum in  $La(NO_3)_3 \cdot xH_2O$ . The sample (around 17 mg) was put in a quartz pan located in a microbalance. Then controlled gas flows with different temperature ranges were introduced and the weight change was recorded continuously. Gas flow and temperature conditions are shown in appendix D.

## 4.4 Catalytic activity test

A schematic sketch of the methane combustion set-up is shown in Figure 4.1. The hydrotalcite-derived catalysts were studied in a quartz fixed bed reactor, see Figure 4.2, where 0.50 g sample (75–150  $\mu$ m) diluted with 2 g  $\alpha$ - $Al_2O_3$  of the same size was loaded into the reactor. The reaction temperature was detected by a thermocouple placed in the middle of the catalyst bed. To get an evaluation of how every catalyst changes over time, a probe of ultraviolet-visible light (UV-Vis) was applied on the middle of the catalyst in the reactor. The furnace with the reactor inside was covered by aluminum foil, in order that the UV-Vis probe was not influenced by the atmosphere light. The furnace was also covered by quartz wool to get the reaction temperature as stable as possible. The UV-Vis spectras were recorded by AvaSpec-3648 spectrometer instrument by AVANTES. An online gas chromatography and mass spectrometer were used to analyze the product gases.

For *in situ* reduction, catalysts were heated from room temperature to 670 °C at heating rate of 2 °C/min in a mixture 75 mL/min  $H_2$  and 75 mL/min Ar (150 mL/min). The reduction was held for 16 h at atmospheric pressure. After reduction the reactor was cooled down to 150 °C using a ramping rate of 5 °C/min. Then the experimental set-up was flushed with inert gas (Ar) for 45 min to clean up hydrogen gas in the set-up. The total combustion of methane was carried out at 150-500 °C. 150 mL/min flow with methane to oxygen ratio at 1:3, whereby 1.5 mL/min  $CH_4$ , 7.5 mL/min 50 %  $O_2$ /Ar and 142 mL/min Ar was introduced into the reactor.

The reaction temperature was then increased to 500 °C with ramping rate of 2 °C/min with

step of 50 °C. For stability test the methane combustion reaction was kept at 500 °C for 2-3 h.

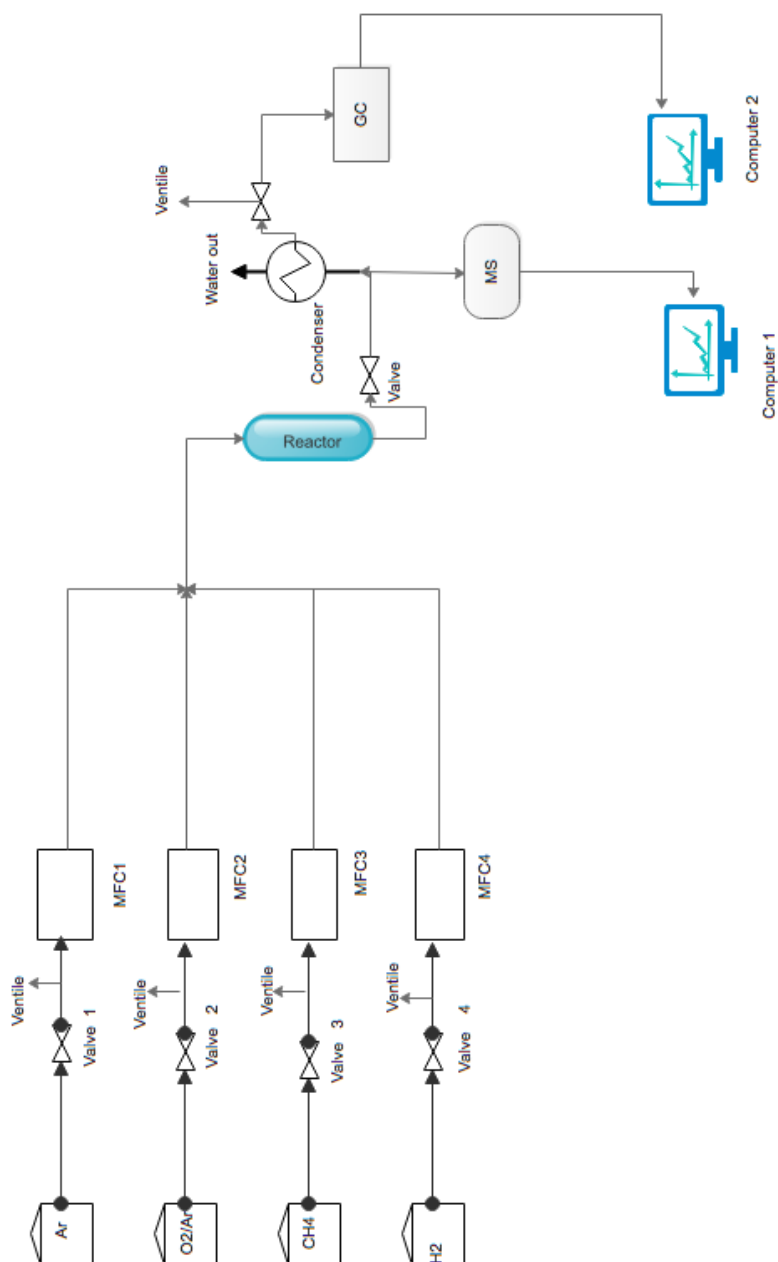


**Figure 4.1:** Schematic sketch of the Set-up for the methane combustion. MFC is Mass Flow controller, MS is mass spectrometer and GC is Gas Chromatography.



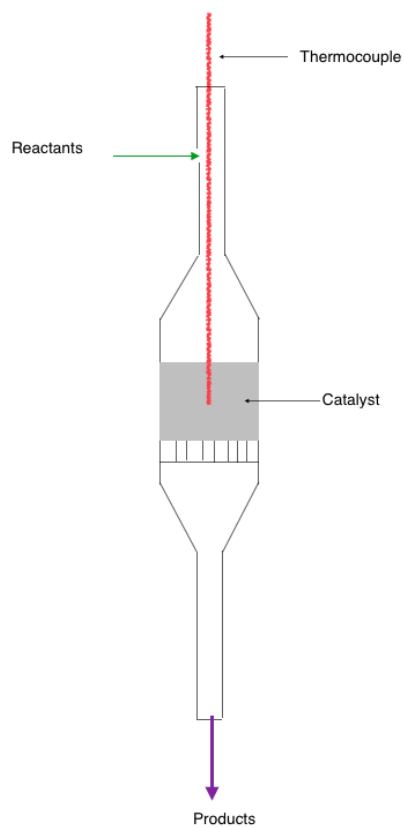


**Figure 4.2:** Schematic sketch of the quartz reactor used for the methane combustion.



# Results and discussion

## 5.1 Catalyst characterization

The results obtained from the characterization procedures are presented and discussed in section 5.1.1–5.1.6.

### 5.1.1 X-Ray Diffraction (XRD)

In this thesis, XRD was performed to get structure insight about the HT catalysts. [Figure 5.1](#) shows the XRD patterns of the uncalcined (dried only) catalysts, while [Figure 5.3](#) shows XRD patterns for the calcined. The uncalcined catalysts (12Co, 3.6Ni-8.4Co) have crystalline structures from  $\theta=11^\circ$  to  $\theta=35^\circ$ , as shown in [Figure 5.1](#). These structures belong to (003), (006) and (009) crystal planes which are characteristic crystalline patterns for hydrotalcite compounds [7, 23]. Crystal planes (012), (015) and (018) are found at the angle positions  $35^\circ$ ,  $38^\circ$  and  $46^\circ$  respectively [23]. These crystal planes are showing the asymmetry and amorphous shapes of the hydrotalcite compounds in these samples and are characteristic for hydroxide double-shaped structures in hydrotalcite-like compounds [18].

The sample of 3.6Ni-8.4Co has sharper peaks than 12Co catalyst. Indeed,  $Ni^{2+}$  has ion radius of 0.72 which is closer to  $Mg^{2+}$  (0.65) and  $Al^{3+}$  (0.60) than  $Co^{2+}$  (0.74). Therefore, cobalt decreases the crystallinity for HT particles, since it is large and therefore difficult to incorporate into the HT structures, while nickel particles are relatively easier to incorporate into the HT lattice [23]. For the dried bimetallic sample (3.6Ni-8.4Co), there is a sharp peak at angle around  $37^\circ$ . This is an error sourced from the sample preparation

for the XRD-characterization.

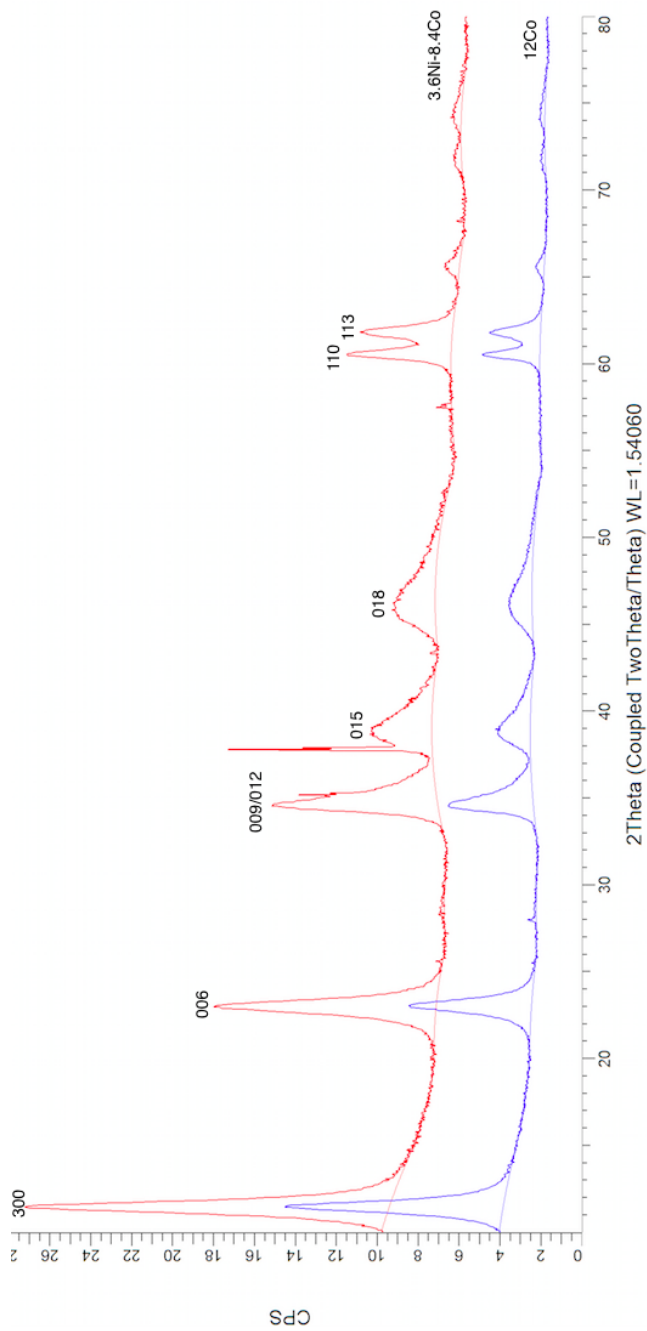


**Figure 5.1:** XRD patterns for uncalcined samples, dried at 70 °C for 10 h.

The catalysts were reduced and passivated under specific conditions to preferentially deposit La promoter onto the metals. The reduced and passivated catalysts were therefore analyzed by XRD to examine the formation of metallic nickel and cobalt. Figure 5.2 shows the results from the XRD. Indeed, significant amounts of metallic nickel and very low metallic cobalt are formed, which are confirmed by the diffraction lines at  $2\theta=44.4^\circ$ ,  $52^\circ$ ,  $76.3^\circ$ .

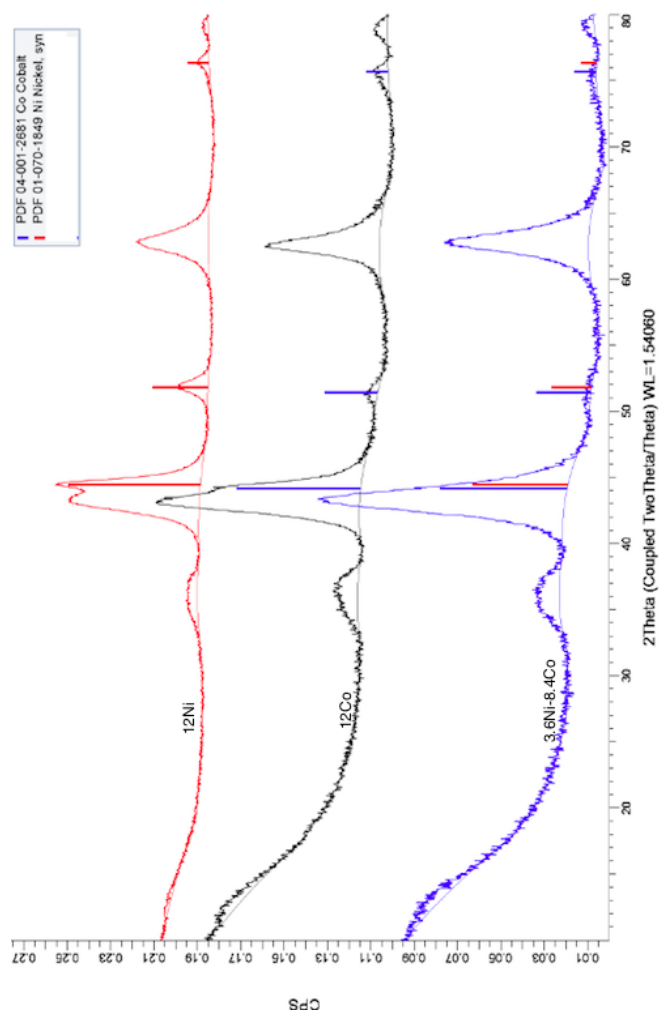


**Figure 5.2:** The XRD patterns for reduced/passivated catalysts. Reduction:  $75 \text{ mL/min } H_2$  and  $75 \text{ mL/min } He$  at  $670^\circ$  for 16 h. Passivation:  $100 \text{ mL/min } 1\% O_2/Ar$  at room temperature for 2 h. The vertical lines shows  $NiO$  and  $CoO$ .

Figure 5.3 shows XRD patterns for the calcined promoted and nonpromoted catalysts. When the dried samples are calcined the hydrotalcite structures disappear. HT compounds are converted to metal oxides, where NiO, CoO and MgO were identified and  $Co_3O_4$  was hardly identified. The spinel phases ( $Al_2MgO_4$ ,  $NiAl_2O_4$ ,  $Co_3O_4$ ,  $CoAl_2O_4$ ,  $MgCo_2O_4$  and  $NiCo_2O_4$ ) were observed by Li He [23] and are not distinguishable, since they are overlapping each other. Lanthanum ( $La_2O_3$ ) has not been shown up in the peak identifications, suggesting that lanthanum species could be well dispersed over the hydrotalcite support or could exist together with  $NiO/Co_3O_4$  matrix undetectable by XRD [44]. Moreover, XRD does not detect the compounds that are presented in small amounts (1–2 %).

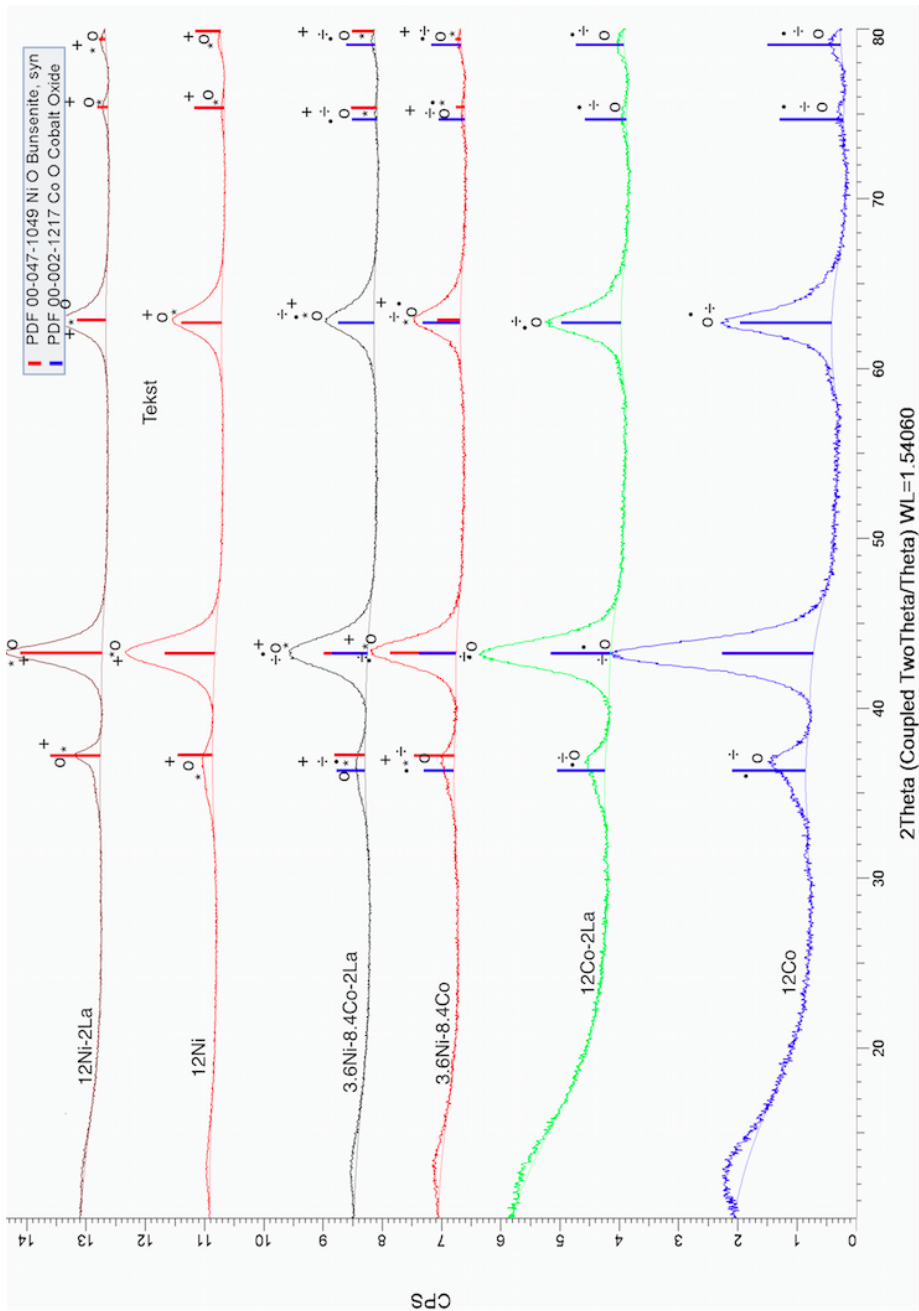


**Figure 5.3:** XRD patterns for calcined samples, calcined at 600 °C for 6 h. ° represent  $MgO$  and  $Al_2MgO_4$ , ★ :  $NiAl_2O_4$ , ◐ :  $Co_3O_4$ ,  $CoAl_2O_4$ , ● :  $MgCo_2O_4$  and + :  $NiCo_2O_4$  [23].

### 5.1.2 X-Ray Fluorescence (XRF)

The calcined catalysts were examined by XRF for elemental analysis and the results are presented in Table 5.1. From this table, it is clear that the major chemical compositions are  $MgO$ ,  $Al_2O_3$ ,  $Co_2O_3$  and  $NiO$ , while the rest are in small amounts, where  $La_2O_3$  is the promoter. However, these values do not agree with the theoretical values. For instance, 12 % Co in the theoretic calculation is found as 6 %, which means the XRF-data are underestimated. Therefore most of the catalysts are further analyzed by ICP-MS (section 5.1.3). It is also observable that the nickel to cobalt ratio from XRF (0.45) is very close to the theoretical ratio (0.43).

**Table 5.1:** The metal oxide compositions of 12Ni, 12Co and 3.6Ni-8.4Co.

Component	Weight percentage (wt.) [%]		
	12Ni	12Co	3.6Ni-8.4Co
$MgO$	67	69	69
$Al_2O_3$	28	25	25
$SiO_2$	0.46	0.32	0.64
$K_2O$	0.24	0.10	0.094
$Co_2O_3$	0.00	6.1	3.6
$NiO$	4.1	0.00	1.3
Nickel to cobalt ratio from XRF	-	-	0.45

To examine if some of the desired components were washed out, the filtration water was also performed on XRF. Table 5.2 shows that none of the desired components were washed off during the catalyst preparation process. In spite of the very low values from XRF analysis, these data are reliable since the main interest in this project is towards getting qualitative information from XRF.

**Table 5.2:** The compositions of filtration water from 12Ni, 12Co and 3.6Ni-8.4Co.

	$Si$ [wt %]	$K$ [wt. %]	$H_2O$ [wt. %]
12Ni	0.04	0.04	99.9
12Co	0.0	0.04	99.9
3.6Ni-8.4Co	0.1	0.03	99.9



### 5.1.3 Inductively Coupled Plasma-Mass Spectrometer (ICP-MS)

The composition of catalysts was analyzed by ICP-MS, since ICP-MS gives accurate elemental analysis. The amounts of *Ni*, *Co* and *La* determined by ICP-MS are listed in Table 5.3. It was found that the actual amounts of the *Ni* in 12Ni catalysts are very close to the nominal values. The amount of *Co* in 12Co is also very close to the nominal value, but 12Co-1La and 12Co-2La have respectively 4.4 % and 3.4 % lower loading than the nominal values. 3.6Ni-8.4Co catalysts have almost correct loading of *Ni*, while the *Co* loading is too high. Indeed, the *Ni* active metal is successfully impregnated into these catalysts. However, the actual amounts of the promoter are much lower than the nominal values which is caused by too low loading of lanthanum nitrate.

**Table 5.3:** The actual amount of the catalysts with or without the promoter.

Catalyst	Weight percentage (wt.) [%]		
	Ni	Co	La
12Ni	13.3	0	
12Ni-1La	13.3	0	0.587
12Ni-2La	13.0	0	1.32
12Co	0	11.6	0
12Co-1La	0	7.70	0.858
12Co-2La	0	8.60	1.47
3.6Ni-8.4Co	3.96	9.58	0
3.6Ni-8.4Co-1La	3.86	8.94	0.698
3.6Ni-8.4Co-2La	3.94	8.82	1.42

### 5.1.4 Nitrogen adsorption

BET surface area, pore volume and pore diameter of the promoted and nonpromoted catalysts obtained from nitrogen adsorption measurement are presented in Table 5.4. The BET surface area of the calcined hydrotalcite-derived catalysts is high and lies within range of 117–176  $m^2/g$  with pore diameter of 8–15  $nm$ . Indeed, this is due to the loss of water and carbon dioxide after calcination of the catalysts [46]. Among the nonpromoted catalysts 3.6Ni-8.4Co shows the highest BET surface area and 12Co has the largest pore volume and pore diameter. Previous reports have shown the same tendency, namely mixed nickel and cobalt oxides have higher surface area than their single oxides [33]. Besides, literature studies have shown HT-derived cobalt catalysts to have higher BET surface area than nickel HT-derived catalysts [33, 35, 36]. Indeed, the explanation why 12Co has almost the same surface area as 12Ni is that the cobalt amount is lower than 12 % as confirmed by

the ICP-MS results (section 5.1.3).

Addition of lanthanum to 12Co and 12Ni decreased the BET surface area with 4.4–13 %, while 3.6Ni-8.4Co catalyst showed 1–4  $m^2/g$  increase in the BET surface area by the La promotion. Lanthanum promoter was supposed to increase the surface area of the nickel catalyst [36, 44, 65], the difference may come from the nature of the support and preparation conditions, such as calcination and reduction temperatures. The observed decreasing BET surface area of 12Co by the La promoter is in accordance with the previous literature studies [21, 22, 35].

The 12Co-2La sample was analyzed three times to determine the instrumental error. The deviation was found to be  $\pm 1.4 m^2/g$  (deviation calculation is found in appendix A.2.1), which means the BET instrumental error is not so large and the obtained surface areas are reliable.

**Table 5.4:** Surface area, pore volume and pore diameter of the calcined catalysts.

Catalyst	$S_{BET} [m^2/g]$	$V_p [cm^3/g]$	$D_p [nm]$
12Co	136	0.461	13.2
12Co-0.5La	125	0.432	13.4
12Co-1La	121	0.467	15.0
12Co-2La	118	0.434	14.4
12Co-2La	118	0.463	15.3
12Co-2La	121	0.474	15.4
12Ni	135	0.397	11.4
12Ni-0.5La	129	0.401	12.1
12Ni-1La	128	0.399	12.2
12Ni-2La	117	0.394	13.1
3.6Ni-8.4Co	172	0.459	10.4
3.6Ni-8.4Co-0.5La	173	0.456	10.1
3.6Ni-8.4Co-1La	176	0.410	8.89
3.6Ni-8.4Co-2La	173	0.444	9.84

The nitrogen adsorption-desorption isotherm plots for nonpromoted catalysts are shown in Figure 5.4. According to IUPAC [17], the shape of these catalysts can be attributed to isotherm type IV and hysteresis loop H3. This shape is characteristic for mesoporous materials ( $2 nm \leq d \leq 50 nm$ ), something that explains why their pore diameter is between 8-15 nm. Indeed, the observed closure point of the hysteresis loop at  $P/P_0 \approx 0.6$  is assigned to the presence of pores open at both ends, which is a characteristic for hydrotalcite derived oxides [27]. The nitrogen adsorption-desorption isotherm plots for all promoted catalysts are given in appendix C.

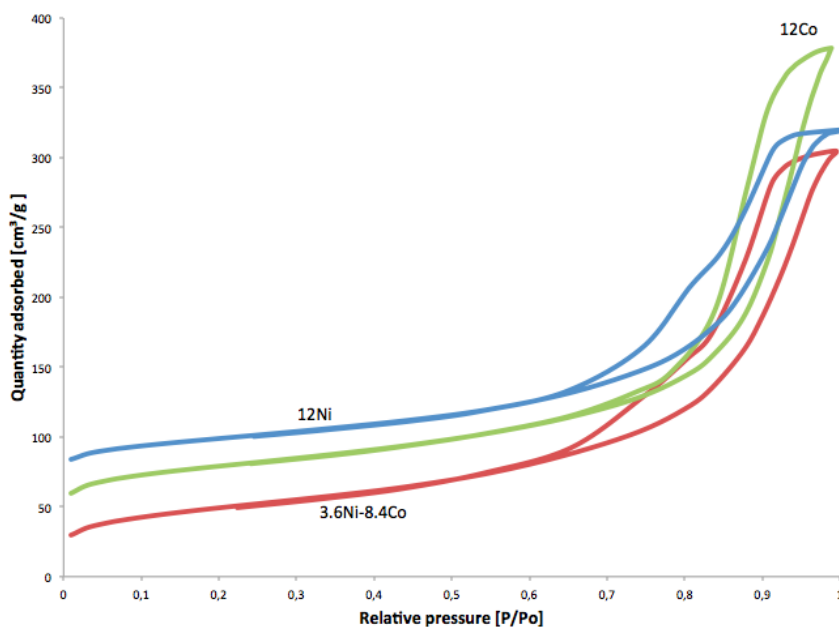


**Figure 5.4:** Nitrogen adsorption-desorption isotherm plots of calcined 12Co, 12Ni and 3.6Ni-8.4Co.

### 5.1.5 Temperature Programmed Reduction (TPR)

The reducibility of catalysts was studied under hydrogen atmosphere. Figure 5.5 presents the TPR patterns of the calcined samples. The results are showing two main reduction peaks at around 400 °C and 800 °C. The region under 400 °C (3.6Ni-8.4Co=322 °C, 12Co=406 °C, 12Co-2La=400 °C 3.6Ni-8.4Co-2La=422 °C and 12Ni-2La=484 °C) carries two explanations. First, for the cobalt contained catalysts, this is attributed to the reduction of  $Co_3O_4$  to  $CoO$  [24]. The second explanation for this region is that the addition of lanthanum to the catalysts increases the hydrogen consumption, so the first reduction peak becomes more observable.

All the samples present peaks around region under 800 °C, which according to the literature are corresponding to the reduction of  $CoO$  to  $Co$  and reduction of  $NiO$  to  $Ni$  [23, 24]. This high reduction temperature explains that the interaction between the support and the active sites are very strong [23]. The lanthanum promoted nickel catalyst has lower reduction temperature than the pure nickel. This could be assigned to a decreased interaction of Ni with the HT-support [44]. Promotion of 3.6Ni-8.4Co catalyst shifts reduction peak under 400 °C region to higher temperatures, while the peaks under 800 °C region remain the same. Hence, reducibility of 3.6Ni-8.4Co samples have been decreased by the

La promotion. 12Co-2La and 12Co-1La are less reduced than their own pure catalyst, since their peaks are shifted towards higher temperature under region at 800 °C, which can be explained as an effect from the La promoter. Overall, the catalysts have unending reduction peaks, corresponding to difficult reductions of periclase (MgO) and spinel ((Co, Ni)Al<sub>2</sub>O<sub>4</sub>..) structures [36].

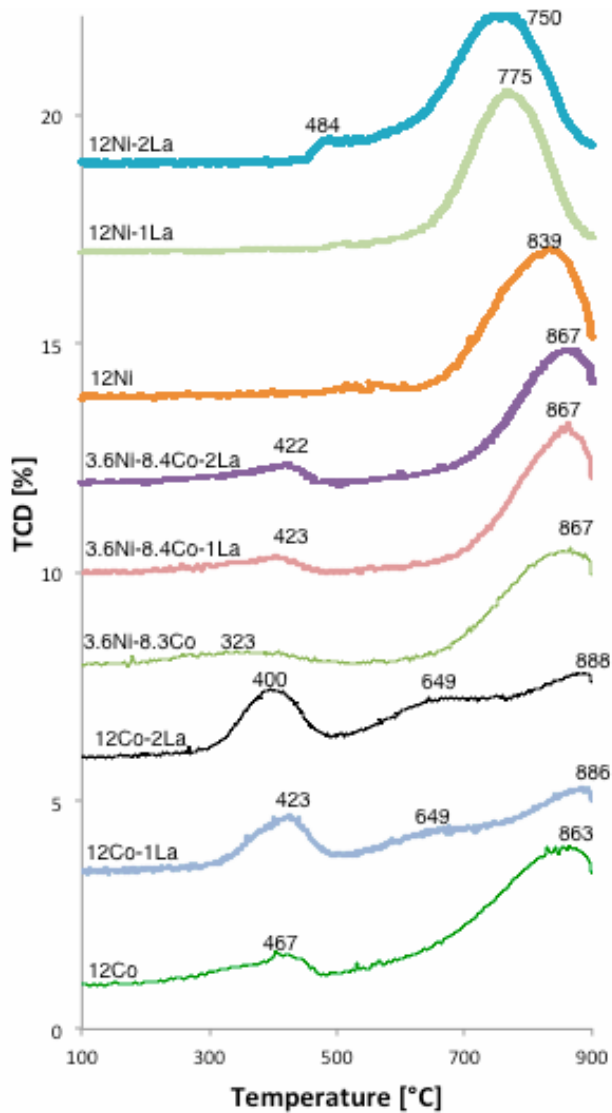


**Figure 5.5:** TPR patterns of calcined samples. Conditions: 100 mg catalyst reduced with 7 % H<sub>2</sub>/Ar at ramping rate of 10 °C.

### 5.1.6 Hydrogen chemisorption

Hydrogen chemisorption was performed on calcined catalysts to determine the metal dispersion (D) and metallic surface area (MSA). The metal dispersion, metallic surface area and the ratio between metallic surface area and BET surface area are presented in Table 5.5, while hydrogen chemisorption isotherms are given in appendix C. All the catalysts show quite good dispersion (5.2–7.4 %), although the spinel structures such as  $NiAl_2O_4$  and  $CoAl_2O_4$  are difficult to reduce [44].

It is seen from the table that 12Ni is mostly dispersed (7.4 %) among the all catalysts, because nickel has higher reducibility than cobalt as the TPR results have shown (section 5.1.5). The lanthanum promotion decreases the dispersion and the metallic surface area, where the decrease is pronounced mostly with 12Co-2La. The ratio between metallic surface area and BET surface area decreases with the lanthanum addition to the catalysts, this could be assigned to that lanthanum covers or blocks parts of the active sites of nickel and cobalt for the hydrogen adsorption. If lanthanum all located on the Ni surface, 23.3 % of Ni surface is covered/blocked by La, as calculations show in appendix A.3.2.

The lanthanum loading is lower than the desired loading amount as the ICP-MS data have shown (5.1.3). If lanthanum was loaded correctly, larger changes of dispersion could be observed.

**Table 5.5:** The metal dispersion (D) and metallic surface area (MSA) of the calcined catalysts.

Catalyst	D [%]	MSA [ $m^2/g$ metal]	ratio <sup>a</sup>
12Co	6.4	43	0.308
12Co-1La	6.4	44	0.364
12Co-2La	5.2	25	0.287
12Ni	7.4	50	0.370
12Ni-1La	5.4	36	0.281
12Ni-2La	5.5	37	0.274
3.6Ni-8.4Co	7.1	48	0.279
3.6Ni-8.4Co-1La	6.2	42	0.239
3.6Ni-8.4Co-2La	6.9	46	0.266

<sup>a</sup> : The ratio between metallic surface area and BET surface area

## 5.2 Catalytic activity results

Catalytic activity results were obtained by methane combustion over different hydrotalcite-derived catalysts. First, the nonpromoted catalysts were tested, then the 2 % La promoted catalysts were tested. It was observed that 2 % La promoted catalysts behave like the nonpromoted catalysts. Therefore, activity test of 0.5–1 % La promoted catalysts was not performed. The following sections discuss the catalytic activity test analysis.

### 5.2.1 UV-Vis evaluation of the catalysts

UV-Vis measurements were performed to study the oxidation states of the active metals in the catalysts. The UV-Vis data for 12Ni are normalized. When the normalization of the UV-Vis spectra data was calculated, a few assumptions were made:

Oxidation fraction depends upon both the oxidation state itself and the temperature, which are important to take into account while calculating the oxidation state fraction. Indeed, before the reduction, the catalyst is 100 % oxidized, as the temperature increases during reduction conditions, it is reduced more and more due to increase of reduction state and temperature. At the end of the reduction and during the cooling temperature, the oxidation state is only function of temperature, meaning the catalyst is totally in reduced form. The following equation was used for the normalization:

$$f = \frac{R_i - R_{min}}{R_{max} - R_{min}} \quad (5.1)$$

, where  $f$  is the oxidation state fraction,  $R_i$  is the reflectance from the oxidation state at different temperatures,  $R_{min}$  is the reflectance of the oxidation state where the catalyst is 100 % reduced at cooling temperature and  $R_{max}$  is the reflectance of the maximum oxidation state referring to when the catalyst is 100 % oxidized. The intensity spectra or reflectance was chosen from wavelength at 540 nm, since the reflectance intensities are most stable in this region and do not display large deviation. The reflectance intensity at various reaction temperatures were normalized and the oxidation state fraction was obtained by [Equation 5.1](#). Calculation of [Equation 5.1](#) and detailed assumptions are found in [appendix A.2.2](#).

The percentage of the oxidation state plotted against the reaction temperature during the methane combustion over 12Ni and 12Ni-2La catalysts is given in [Figure 5.6](#). Indeed, the oxidation state does not increase significantly until the reaction temperature is 300 °C. From 300 °C to 500 °C, the oxidation state of both catalysts increases with increased temperature.

It is also seen from the figure that the oxidation state of 12Ni is higher than the one for 12Ni-2La, which can confirm that lanthanum keeps the catalyst in more reduced form.

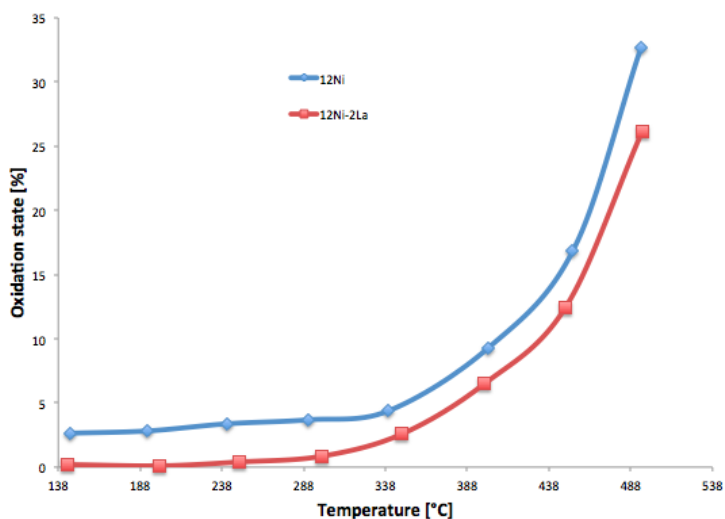


**Figure 5.6:** Oxidation state vs. bed temperature for 12Ni and 12Ni-2La during methane combustion. Reaction conditions: 0.5 g catalyst diluted with 2 g  $\alpha$ - $Al_2O_3$ , 1.5 mL/min  $CH_4$ , 7.5 mL/min 50 %  $O_2/Ar$  and 142 mL/min  $Ar$  at 150–500 °C with ramping rate of 2 °C/min .

The cobalt-contained catalysts showed complex spectra and hence have not been normalized. Figure 5.7 shows the reflectance of 12Co displayed both during the reduction step and the methane combustion. It is observed that during the reduction step, the reflectance intensity decreases. During the methane combustion, the opposite is observed, namely the reflectance intensity increases with the reaction temperature. The complexity cobalt contained catalysts have shown is based on two tendencies. The reflectance intensity increases from room temperature to around 500 °C and then decreases to around 660 °C. Indeed, the hydrotalcite-derived cobalt catalysts contains spinel cobalt oxides [7, 32] as the XRD patterns have confirmed, meaning  $Co^{3+}$  and  $Co^{2+}$  ions are presented in the catalyst. The UV-Vis reflectance spectra can consequently be assigned to transition from  $Co^{3+}$  to  $Co^{2+}$  in the first tendency of the reduction step, followed by the shift of  $Co^{2+}$  to  $Co^0$  in the second tendency of the reduction step.

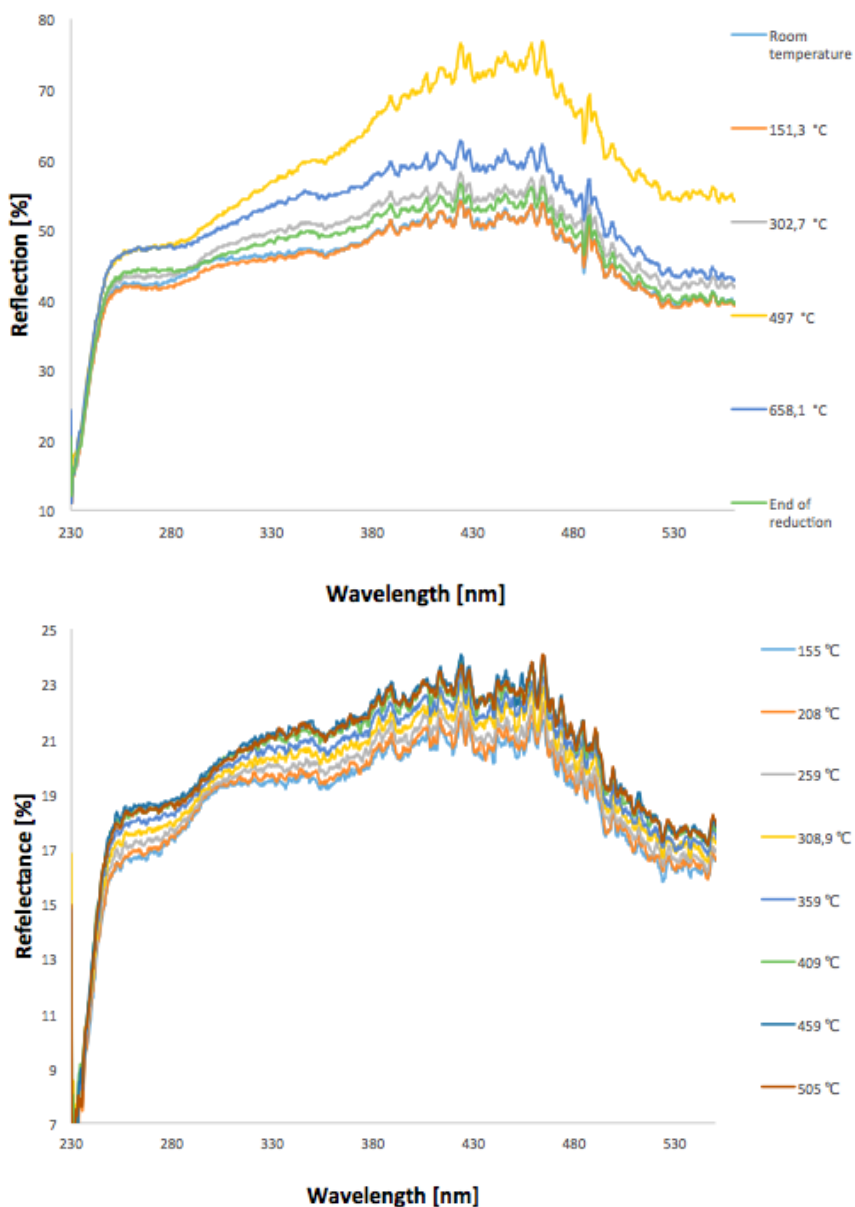


**Figure 5.7:** UV-Vis spectra of 12Co catalysts during reduction step (top) and methane combustion (bottom) at different temperatures. Reaction conditions: 0.5 g catalyst diluted with 2 g  $\alpha$ - $Al_2O_3$ . Top : 75 mL/min  $H_2$ , 75 mL/min Ar at from room temperature to 670 °C with ramping rate of 2 °C/min, isotherm treatment at 670 °C for 16 h. Bottom : 1.5 mL/min  $CH_4$ , 7.5 mL/min 50 %  $O_2$ /Ar and 142 mL/min Ar at 150–500 °C with ramping rate of 2 °C/min, where the catalyst was first reduced.



Figure 5.8 shows the reflectance intensity of 12Ni during the reduction step, where the reflectance decreases with the temperature all the time. Indeed, 12Ni catalyst does not demonstrate such oscillation cobalt catalyst has shown, meaning only the transition of  $Ni^{2+}$  to  $Ni^0$  is present.

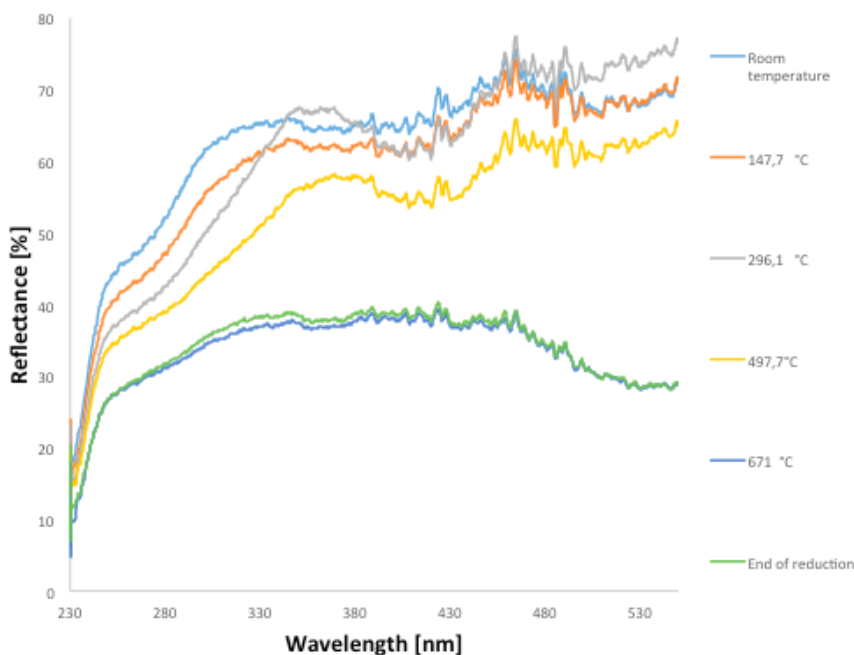


**Figure 5.8:** UV-Vis spectra of 12Ni catalysts during reduction step at different temperatures. Reaction conditions: 0.5 g catalyst diluted with 2 g  $\alpha-Al_2O_3$ , 75 mL/min  $H_2$ , 75 mL/min  $Ar$  at from room temperature to 670 °C with ramping rate of 2 °C/min, isotherm treatment at 670 °C for 16 h

## 5.2.2 Methane conversion and catalyst stability

The catalyst activity test was performed based on studying the methane conversion variation at different temperatures using different hydrotalcite-derived catalysts. The activity test of promoted and nonpromoted catalysts is shown in Figure 5.9. The methane conversion is seen to increase with the reaction temperature on all the catalysts. Overall, the cobalt contained catalysts gave higher activity than the 12Ni catalysts and none of the catalysts has complete conversion of methane. According to the literature, cobalt exhibits weak oxygen bond strength and high turnover frequency for redox reactions [33], due to the low bulk heat of formation of cobalt oxide.

Thus, the ease of removal of oxygen from cobalt oxide gives higher methane conversion. Easy release of oxygen results to more oxygen which is important for reaction mechanisms in methane decomposition. [52, 55]

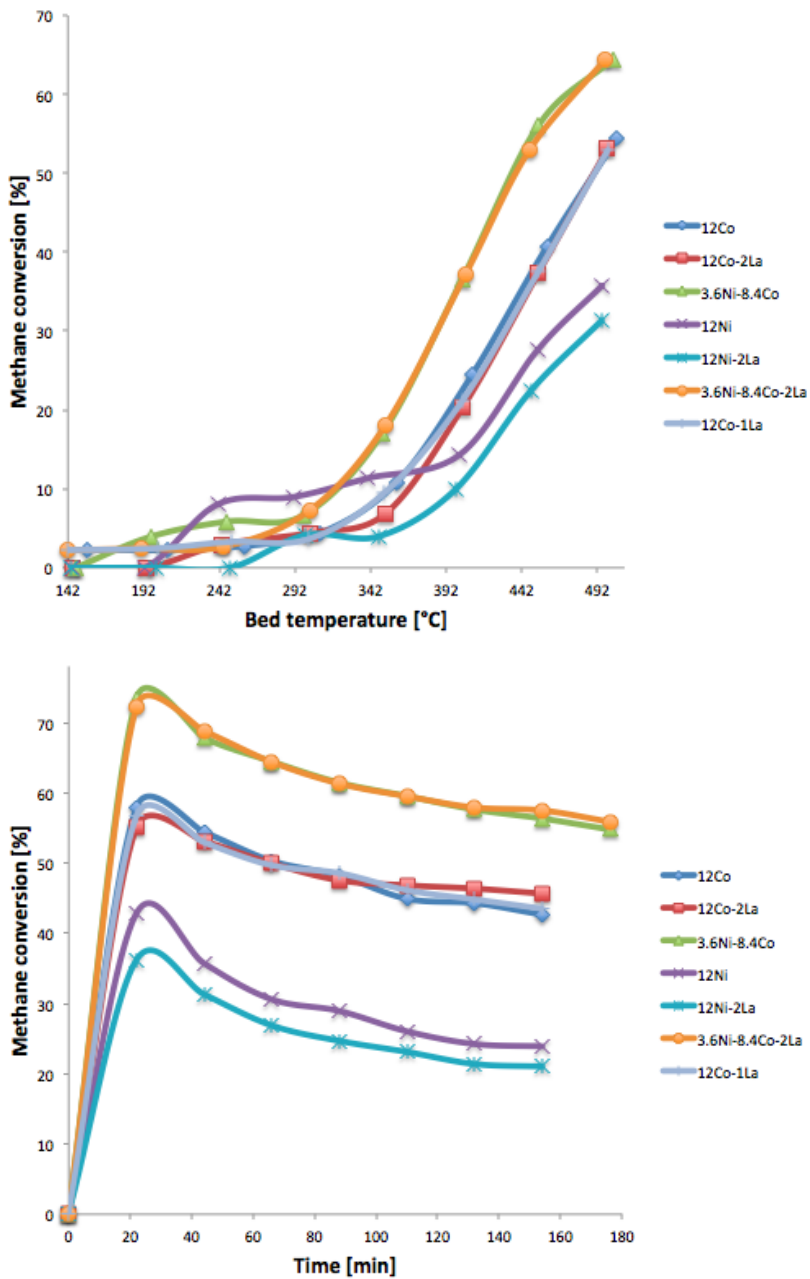
12Co showed lower methane conversion than 3.6Ni-8.4Co catalyst, because the actual amount of cobalt in 3.6Ni-8.4Co is quite high based on the ICP-MS results (section 5.1.3). It is also important to mention that Ni-Co mixed oxides have better catalytic performance than their own single oxides [33], which may be the reason why 3.6Ni-8.4Co has higher activity than 12Co.

It turned out that promotion did not give significant changes on the methane conversion, except from 12Ni-2La which showed slightly lower activity than 12Ni, which is possibly assigned to reduced oxidation state fraction of Ni. Indeed, the activity of 12Ni decreased with the addition of the lanthanum, which is also possibly due to the blockage/coverage effect of lanthanum on the active sites of nickel as the dispersion data shows in Table 5.5. However, catalyst activity is increased by La addition. In one hand, lanthanum reduces the number of active sites. On the other hand, it increases the remaining active site. Therefore, lanthanum compensates catalyst activity and the methane conversion of the nonpromoted and promoted catalysts is the same.

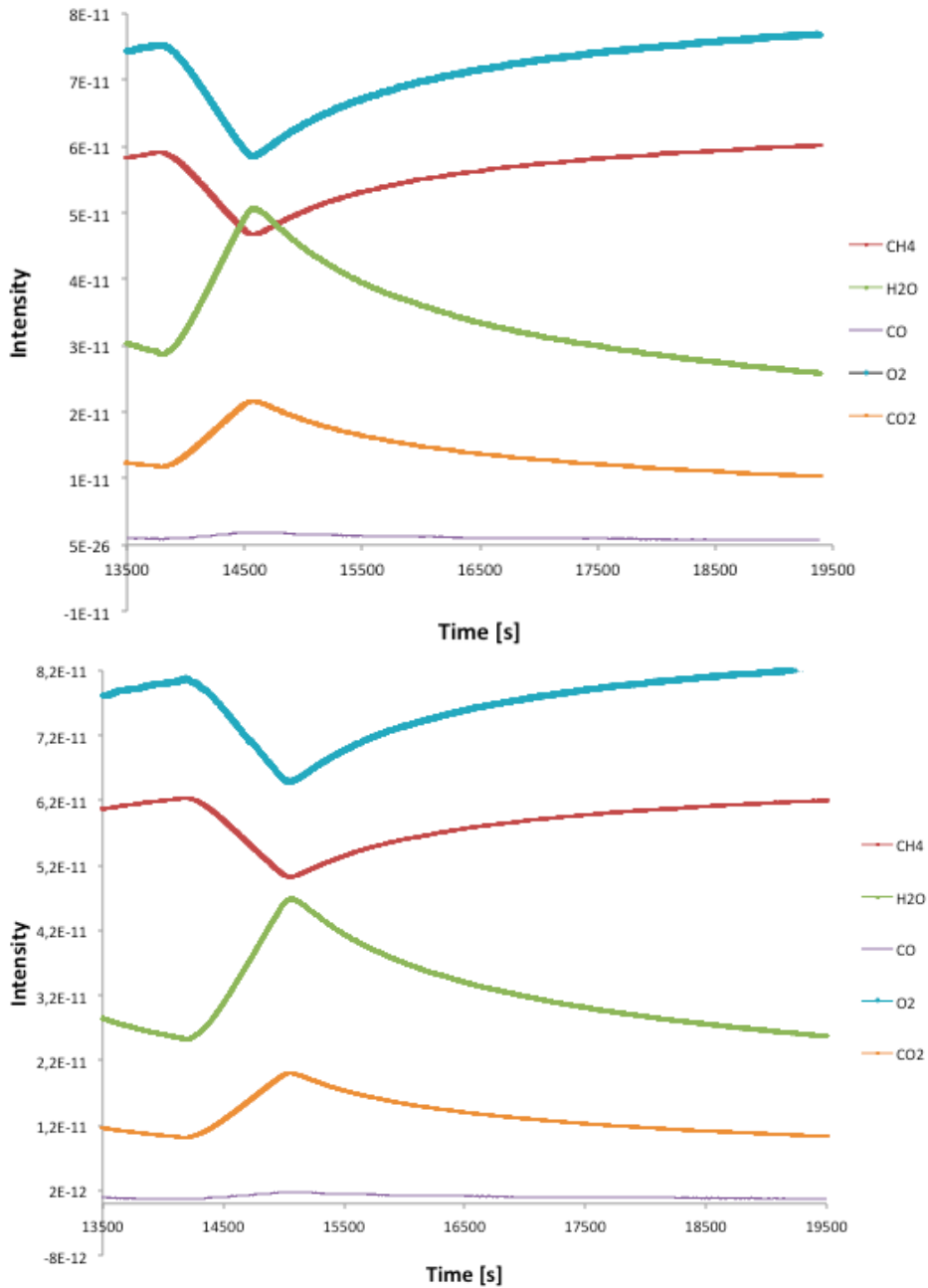
For catalyst stability study, the catalysts were studied at 500 °C for 2 h under the same reaction conditions and results are given in the bottom part in Figure 5.9. At the temperature of around 500 °C all the catalysts exhibit the highest conversion of methane. Still the promoted catalysts perform the same as nonpromoted ones, except from 12Ni-2La which shows slightly lower activity than 12Ni. However, the methane conversion decreases over time, which is mostly due to the catalyst deactivation observed from the MS-data.

Figure 5.10 shows both the reactants and products of the total methane combustion over 12Ni and 12Ni-2La at 500 °C (the same figures for the other catalysts is found in appendices C.13 and C.14). It is seen from this figure that after the reaction has reached the highest methane conversion, the reactants increase little by little while the products are decreasing significantly, meaning that the activity loss of catalysts has started. At this temperature, the deactivation of the catalyst might happen due to sintering of the catalysts and/or carbon formation on the catalysts and was investigated further.

Figure 5.10 shows that CO is formed in small amounts even though this was not detected by the GC.



**Figure 5.9:** Reaction conditions: 0.5 g catalyst diluted with 2 g  $\alpha\text{-Al}_2\text{O}_3$ , 1.5 mL/min  $\text{CH}_4$ , 7.5 mL/min 50 %  $\text{O}_2/\text{Ar}$  and 142 mL/min Ar with ramping rate of 2 °C/min. Top : Methane conversion vs. temperature. Bottom : Methane conversion at 500 °C.



**Figure 5.10:** The MS-intensity as function of time during the isothermal (500 °C) combustion of methane. Reaction conditions: 0.5 g catalyst diluted with 2 g  $\alpha$ - $Al_2O_3$ , 1.5 mL/min  $CH_4$ , 7.5 mL/min 50 %  $O_2$ /Ar and 142 mL/min Ar.

Top: 2Ni, bottom: 12Ni-2La.

### 5.2.3 Deactivation of the catalysts

The deactivation observed during the methane combustion was investigated further, assuming that the deactivation could happen due to sintering and/or carbon formation. Sintering is the process where small nickel or cobalt particles form bigger sized particles, which causes less active sites on the surface area. Sintering leads therefore to less activity [46]. Indeed, sintering is favored at high temperatures and the presence of water, where the latter one is present in methane combustion [4, 46].

Sintering was investigated by measuring the spent catalysts in chemisorption, where the spent catalysts of 12Co-2La and 12Ni-2La were measured. Reduction conditions were changed to avoid sintering during the reduction process. The samples were reduced at 400 °C for 3 h assuming that  $\alpha\text{-Al}_2\text{O}_3$  does not contribute to chemisorption.

Results from the  $H_2$  chemisorption on the spent catalysts are given in Table 5.6. Both the metal dispersion and the metallic surface area are higher than those for the fresh catalysts. Sajjanikumari Sadasivan [47] observed re-dispersion process during re-reduction of the oxidized large cobalt particles, where the particles fragmented into smaller particles on reduction. Hence, the increase of the dispersion is probably caused by re-dispersion and sintering is not a part of deactivation factors.

**Table 5.6:** The metal dispersion (D) and metallic surface area (MSA) of the calcined catalysts before and after methane combustion reaction.

Catalyst	Fresh		Spent	
	D [%]	MSA [ $m^2/g$ ]	D [%]	MSA [ $m^2/g$ ]
12Co-2La	5.2	25	7.4	50
12Ni-2La	5.5	37	6.3	42

On the other hand, there could be carbon formation on the catalyst support which deactivates the active sites. The carbon formation process occurs at high temperature conditions and is accelerated by the sintering process, since larger particles stimulate the carbon formation.[46, 36]

Carbon formation was studied, where the spent catalysts of 12Co, 12Ni and 3.6Ni-8.4Co were measured in the TGA. 15-20 mg of every spent catalyst was heated 10 °C/min from room temperature to 900 °C with 75 mL/min air flow. A detailed file about the gas flows and isotherm conditions is given in D.2. Then the weight change as a function of the temperature was recorded and MS was connected to the TGA to detect carbon dioxide.

The TGA results are confirming that carbon formation is one of the deactivation factors, since carbon dioxide ( $CO_2$ ) has been detected by the MS as seen from Figure 5.11,

where the following reaction is assumed to take place:



Figure 5.11 is illustrating that 12Co has highest carbon deposition, since it displays largest carbon dioxide. However, the literature studies have shown nickel catalysts to have higher carbon deposition than cobalt catalysts [35, 36]. Hence, further investigations are needed to decide which catalyst that is mostly destabilized by carbon formation.

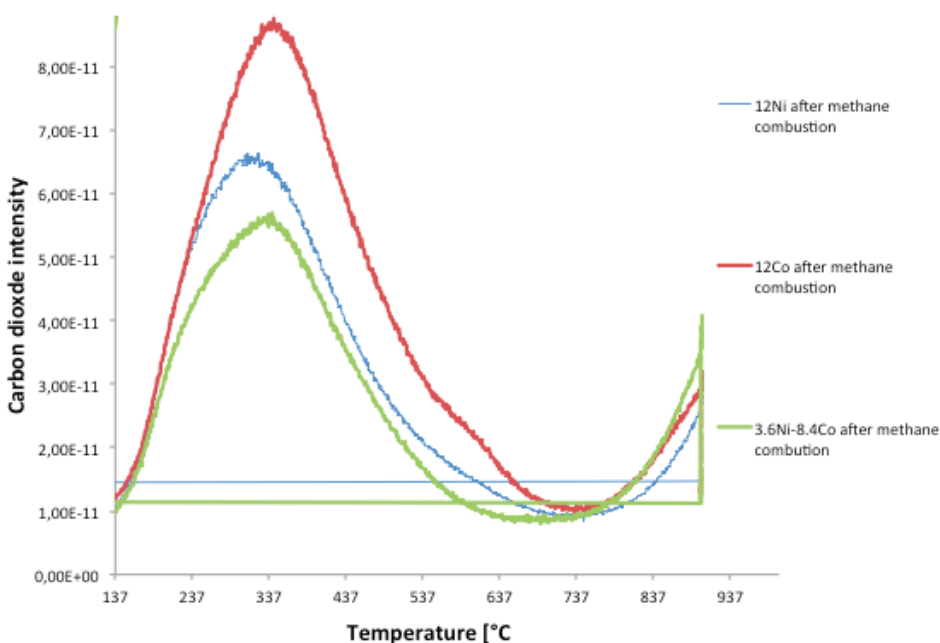


**Figure 5.11:** MS intensity of  $CO_2$  of the spent catalysts as a function of temperature. Conditions: 15-20 mg spent catalyst after methane combustion, heated  $10\text{ }^\circ\text{C}/\text{min}$  from room temperature to  $900\text{ }^\circ\text{C}$  with  $75\text{ mL}/\text{min}$  air flow and  $25\text{ mL}/\text{min}$  Ar and isotherm treatment at  $900\text{ }^\circ\text{C}$  for 3 h.

Rate of carbon formation (C-formation) of the catalysts after methane combustion is given in table Table 5.7. All the catalysts have quite similar rate of carbon formation, where the difference is associated with the duration of methane combustion reactions. The TGA experiments could be repeated to decide the instrumental error, and hence evaluate if the rate difference is also originated from the instrument.

**Table 5.7:** Carbon formation of spent catalysts measured by TGA.

Catalyst	C-formation [ <i>mg/h</i> ]
12Co	0.092
12Ni	0.086
3.6Ni-8.4Co	0.092





## Conclusion

12Ni, 12Co and 3.6Ni-8.4Co catalysts were derived from hydrotalcite-like compounds by co-precipitation method and promoted with lanthanum (La) by incipient wetness impregnation method. It turned out that 12Ni had higher reducibility and dispersion but lower BET surface area than 12Co and 3.6Ni-8.4Co catalyst.

When hydrotalcite-derived catalysts were promoted with small amounts of lanthanum, changes happened in terms of reducibility, dispersion and surface area. Indeed, the dispersion decreased with the addition of lanthanum for all of the catalysts. Reducibility decreased for the cobalt-contained catalysts and increased for 12Ni catalysts. 3.6Ni-8.4Co catalyst got 0.6–5 % higher BET surface area while other catalysts showed 4.4–13 % lower BET surface. Promotion of the catalysts with small amounts of La has not had remarkable changes on the catalytic activity. However, 12Ni-2La showed a lower activity, which is possibly assigned to the blockage/coverage effect of lanthanum on the active sites of nickel, as well as reduced oxidation state fraction of Ni. The spent catalysts re-dispersed during re-reduction of oxidized large particles, where the particles may be fragmented into smaller particles on reduction. Moreover, carbon formation was observed to be a main deactivation factor.

It could be concluded that 3.6Ni-8.4Co is the most active catalyst based on the methane conversion. Furthermore, lanthanum had two effects on the hydrotalcite-derived nickel and cobalt catalysts, namely; it blocked/covered partially the active sites of cobalt and nickel and it kept the catalysts in reduced form on the basis of the UV-Vis evaluation of the catalysts. Moreover, lanthanum did not improve the methane conversion, but it possibly enhances the activity. In view of the hydrogen chemisorption results, lanthanum reduced number of active sites and increased the remaining active sites at the same time.



## Further research

Here are some important recommendations that could improve this research project. To determine the reason why 3.6Ni-8.4Co catalyst showed the highest methane conversion, SEM (Scanning Electron Microscopy) can be used to study the micro-structure of the catalyst, something that could tell if the active sites got bimetallic dispersion on the support. To get the correct loading of lanthanum on the catalysts, a lanthanum(III) nitrate hydrate with known hydrate amount can be purchased as this makes it easier to calculate the number of moles of lanthanum, hence avoiding too low loading of lanthanum. A micro-GC can be used to get the carbon monoxide detected, which was not detected by the currently used GC in this project.

In this project work, 12Co with lower loading was obtained, where the low loading is possibly caused by experimental error. This experimental error could be reduced to carry the co-precipitation method more carefully or using other preparation methods such as spray drying technique. Spray drying technique as a catalyst synthesizing method has many advantages. This technique is much more simplified than co-preparation method with short preparation times, as well as reasonable production of high performing nickel and cobalt catalysts. [46]

Based on the previous researches, cerium (Ce) could be substituted with lanthanum, because cerium has shown to have higher activity than lanthanum promotion on nickel and/or cobalt catalysts in oxidation of hydrocarbons and steam reforming process [36, 44, 21, 35]. Adding 1–5 % cerium (Ce) to  $Ni/Al_2O_3$  over the reforming of methane with carbon dioxide has increased reducibility and dispersion of nickel due to reduction of chemical interaction between nickel and the alumina support [44]. Cerium has also the ability to store oxygen in form of  $CeO_2$ , something that can greatly suppress the carbon

deposition [44]. Besides, high oxygen storage is important, since activation of oxygen plays an important role in methane combustion for the surface kinetics controlled region [34].

Activity loss of the catalysts at the steady state temperature was observed and further research and study is needed, to clarify the cause and mechanism of the deactivation. Transition electron microscope (TEM) technique can be performed on the spent catalysts to study the carbon formation. However, an easy way to extract  $\alpha\text{-Al}_2\text{O}_3$  from the catalysts must be determined.

# Bibliography

- [1] A full diagram of a mass spectrometer. <https://www.chemguide.co.uk/analysis/masspec/howitworks.html>. Accessed: 24.04.2018.
- [2] David W. Agar. Multifunctional reactors: Old preconceptions and new dimensions. *Chemical Engineering Science*, 54(10):1299–1305, 1999.
- [3] James A Anderson. Supported metals in catalysis, 2011.
- [4] Morris Argyle and Calvin Bartholomew. Heterogeneous catalyst deactivation and regeneration: A review. *Catalysts*, 5(1):145–269, March 2015.
- [5] Angelo Basile. *Methane in the environment : occurrence, uses and production*. Energy Science, Engineering and Technology. Nova Science Publishers, 2011.
- [6] Andrzej Borodziski and Magdalena Bonarowska. Relation between crystallite size and dispersion on supported metal catalysts. *Langmuir*, 13(21):5613–5620, October 1997.
- [7] F. Cavani, F. Trifir, and A. Vaccari. Hydrotalcite-type anionic clays: Preparation, properties and applications. *Catalysis Today*, 11(2):173–301, 1991.
- [8] Jinghuan Chen, Hamidreza Arandiyani, Xiang Gao, and Junhua Li. Recent advances in catalysts for methane combustion. *Catalysis Surveys from Asia*, 19(3):140–171, September 2015.
- [9] Jinghuan Chen, Xueying Zhang, Hamidreza Arandiyani, Yue Peng, Huazhen Chang, and Junhua Li. Low temperature complete combustion of methane over cobalt chromium oxides catalysts. *Catalysis Today*, 201:12–18, March 2013.

- 
- [10] Jie Cheng, Junjie Yu, Xiaoping Wang, Landong Li, Jinjun Li, and Zhengping Hao. Novel ch<sub>4</sub> combustion catalysts derived from cu-co/x-al (x= fe, mn, la, ce) hydrotalcite-like compounds. *Energy & Fuels*, 22(4):2131–2137, 2008.
- [11] I. Chorkendorff. *Concepts of modern catalysis and kinetics*. Wiley-VCH, Weinheim, 2nd, rev. and enl. ed. edition, 2007.
- [12] T.V Choudhary, S Banerjee, and V.R Choudhary. Catalysts for combustion of methane and lower alkanes. *Applied Catalysis A, General*, 234(1):1–23, 2002.
- [13] Andrzej Cybulski and Jacob A. Mouljin. *Structured catalysts and reactors*, 2006.
- [14] Anh Hoang Dam. *Bimetallic catalyst system for steam reforming*, 2016.
- [15] Sudipta De, Jianguang Zhang, Rafael Luque, and Ning Yan. Ni-based bimetallic heterogeneous catalysts for energy and environmental applications. *Energy & Environmental Science*, 9(11):3314–3347, November 2016.
- [16] D. Dissanayake, M.P. Rosynek, K.C.C. Kharas, and J.H. Lunsford. Partial oxidation of methane to carbon monoxide and hydrogen over a ni/al<sub>2</sub>o<sub>3</sub> catalyst. *Journal of Catalysis*, 132(1):117–127, 1991.
- [17] G. Ertl, H. Knzinger, and J. Weitkamp. *Handbook of Heterogeneous Catalysis*, volume 1-5. Wiley-VCH Verlag GmbH, April 2008.
- [18] Javier Feroso, María V Gil, Fernando Rubiera, and De Chen. Multifunctional pd/ni-co catalyst for hydrogen production by chemical looping coupled with steam reforming of acetic acid. *ChemSusChem*, 7(11):3063–3077, 2014.
- [19] Y. Gou, X. Liang, and B. Chen. Porous ni-co bimetal oxides nanosheets and catalytic properties for co oxidation. *Journal of Alloys and Compounds*, 574:181–187, 2013.
- [20] R. Guerrero-Lemus and L.E. Shephard. Natural gas. In *Lecture Notes in Energy*, volume 38, pages 323–343. Springer Verlag, 2017.
- [21] P. Chaumette HB. Ernstl, A. Kiennemannl. Comparative studies of lanthanum and cerium as promoters of cobalt based fischer-tropsch catalysts.
- [22] Leilei He, Yulong Botaoteng, Maohong Zhang, and Maohong Fan. Development of composited rare-earth promoted cobalt-based fischertropsch synthesis catalysts with high activity and selectivity. *Applied Catalysis A, General*, 505:276–283, September 2015.

- 
- [23] Li He, Helene Berntsen, Esther Ochoa-Fernandez, John Walmsley, Edd Blekkan, and De Chen. Coni catalysts derived from hydrotalcite-like materials for hydrogen production by ethanol steam reforming. *Topics in Catalysis*, 52(3):206–217, April 2009.
- [24] Zhiwei Huang, Fang Cui, Haixiao Kang, Jing Chen, and Chungu Xia. Characterization and catalytic properties of the cuo/sio<sub>2</sub> catalysts prepared by precipitation-gel method in the hydrogenolysis of glycerol to 1,2-propanediol: Effect of residual sodium. *Applied Catalysis A, General*, 366(2):288–298, 2009.
- [25] International Energy Agency (IEA). Energy sector methane recovery and use. *SPE Journal*, page page 3, 2009.
- [26] Abdullah Irankhah, Mehri Rahimi, and Mehran Rezaei. Performance research on a methane compact reformer integrated with catalytic combustion. *Chemical Engineering & Technology*, 37(7):1220–1226, July 2014.
- [27] Zheng Jiang, Junjie Yu, Jie Cheng, Tiancun Xiao, Martin Jones, Zhengping Hao, and Peter Edwards. Catalytic combustion of methane over mixed oxides derived from co-mg/al ternary hydrotalcites. *Fuel Processing Technology*, 91(1):97–102, January 2010.
- [28] N. Kamiuchi and K. Eguchi. Catalytic combustion of methane. In *Catalysis for Alternative Energy Generation*, volume 9781461403449, pages 305–327. Springer New York, April 2012.
- [29] Charles Kittel. *Introduction to solid state physics*. Wiley, Hoboken, N.J, 8th ed. edition, 2005.
- [30] Ertl G. Knzinger H., Weitkamp J., editor. *Handbook of heterogeneous catalysis*. VCH, 1997.
- [31] Y. Kobayashi, J. Horiguchi, S. Kobayashi, Y. Yamazaki, K. Omata, D. Nagao, M. Konno, and M. Yamada. Effect of nio content in mesoporous nio-al<sub>2</sub>o<sub>3</sub> catalysts for high pressure partial oxidation of methane to syngas. *Applied Catalysis A: General*, 395(1-2):129–137, March 2011.
- [32] Joo H. Lee and David L. Trimm. Catalytic combustion of methane. *Fuel Processing Technology*, 42(2):339–359, 1995.
- [33] Tae Hwan Lim, Sung June Cho, Hee Sung Yang, M.H Engelhard, and Do Heui Kim. Effect of co/ni ratios in cobalt nickel mixed oxide catalysts on methane combustion. *Applied Catalysis A, General*, 505:62–69, September 2015.
-

- 
- [34] Fengxiang Liu, Yanyan Sang, Hongwei Ma, Zhanping Li, and Zhiming Gao. Nickel oxide as an effective catalyst for catalytic combustion of methane. *Journal of Natural Gas Science and Engineering*, 41:1–6, May 2017.
- [35] Alessandra F. Lucrdio, Gregory Jerkiewicz, and Elisabete M. Assaf. Cobalt catalysts promoted with cerium and lanthanum applied to partial oxidation of methane reactions. *Applied Catalysis B, Environmental*, 84(1):106–111, 2008.
- [36] Alessandra Fonseca Lucrdio, Gregory Jerkiewicz, and Elisabete Moreira Assaf. Nickel catalysts promoted with cerium and lanthanum to reduce carbon formation in partial oxidation of methane reactions. *Applied Catalysis A, General*, 333(1):90–95, 2007.
- [37] Peter Luger. *Modern X-ray analysis on single crystals : a practical guide*. De Gruyter, 2nd ed. edition, 2014.
- [38] Jack H Lunsford. Catalytic conversion of methane to more useful chemicals and fuels: a challenge for the 21st century. *Catalysis Today*, 63(2):165–174, 2000.
- [39] Rene Margui, Evatvan Grieken. *X-ray fluorescence spectrometry and related techniques: an introduction*. Momentum Press, 2013.
- [40] Harold M McNair. *Basic gas chromatography*. Wiley, Hoboken, N.J, 2nd ed. edition, 2009.
- [41] V.G. Milt, M.A. Ulla, and E.A. Lombardo. Cobalt-containing catalysts for the high-temperature combustion of methane. *Catalysis Letters*, 65(1):67–73, Mar 2000.
- [42] Takanori Miyake and Tetsuo Asakawa. Recently developed catalytic processes with bimetallic catalysts. *Applied Catalysis A, General*, 280(1):47–53, 2005.
- [43] Jacob A. Moulijn. *Chemical process technology*. Wiley, Chichester, 2nd ed. edition, 2013.
- [44] Sittichai Natesakhawat, Okan Oktar, and Umit S. Ozkan. Effect of lanthanide promotion on catalytic performance of solgel ni/al 2o 3 catalysts in steam reforming of propane. *Journal of Molecular Catalysis. A, Chemical*, 241(1):133–146, 2005.
- [45] J. W Niemantsverdriet. *Spectroscopy in catalysis : an introduction*, 2007.
- [46] Tayyaba Noor. *Sorption enhanced high temperature water gas shift reaction : materials and catalysis*, 2013.



- 
- [47] Sajanikumari Sadasivan, Ronan M. Bellabarba, and Robert P. Tooze. Size dependent reductionoxidationreduction behaviour of cobalt oxide nanocrystals. *Nanoscale*, 5(22):11139–11146, October 2013.
- [48] Kaimin Shih. *X-Ray Diffraction: Structure, Principles and Applications*. Materials Science and Technologies. Nova Science Publishers, Inc., Hauppauge, 1900.
- [49] K.S.W. Sing, D.H. Everett, R.A.W. Haul, L. Moscou, R.A. Pierotti, J. Rouquerol, and T. Siemieniewska. Reporting physisorption data for gas/solid systems with special reference to the determination of surface area and porosity. *Pure and Applied Chemistry*, 57(4):603–619, January 1985.
- [50] Douglas A. Skoog. Principles of instrumental analysis, 2007.
- [51] Silviya Todorova, Hristo Kolev, Plamen Stefanov, and Anton Naydenov. Catalytic oxidation of methane over pd-meox (me = mn, co, ni, ce) catalysts - influence of metal oxides. *Revue Roumaine de Chimie*, 59(3-4):251–257, March 2014.
- [52] Weifeng Tu, Mireille Ghossoub, Chandra Veer Singh, and Ya-Huei Cathy Chin. Consequences of surface oxophilicity of ni, ni-co, and co clusters on methane activation. *Journal of the American Chemical Society*, 139(20), 24 2017.
- [53] Jorge A Velasco. *Catalytic partial oxidation of methane over nickel and ruthenium based catalysts for GTL applications*. PhD thesis, KTH Royal Institute of Technology, 2015.
- [54] E. Vinogradova, A. Dulnev, V. Efremov, and E. Golosman. Synthesis of nickelcoppercobalt catalysts for deep oxidation of methane and optimization of their composition. *Russian Journal of Applied Chemistry*, 83(1):84–91, January 2010.
- [55] Ie Wachs and K Routray. Catalysis science of bulk mixed oxides. *Acs Catalysis*, 2(6):1235–1246, June 2012.
- [56] Israel E. Wachs. Recent conceptual advances in the catalysis science of mixed metal oxide catalytic materials. *Catalysis Today*, 100(1):79–94, 2005.
- [57] Bert M. Weckhuysen and Robert A. Schoonheydt. Recent progress in diffuse reflectance spectroscopy of supported metal oxide catalysts. *Catalysis Today*, 49(4):441–451, 1999.
- [58] R.J Wijngaarden. *Industrial catalysis : optimizing catalysts and processes*. Wiley-VCH, Weinheim, 1998.
-

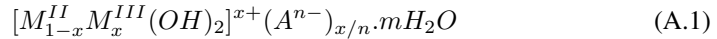
- 
- [59] Tian-Cun Xiao, Sheng-Fu Ji, Hai-Tao Wang, Karl S Coleman, and Malcolm L.H Green. Methane combustion over supported cobalt catalysts. *Journal of Molecular Catalysis. A, Chemical*, 175(1):111–123, 2001.
- [60] Jun Jie Yu, Zheng Jiang, Ling Zhu, Zheng Ping Hao, and Zhi Ping Xu. Adsorption/desorption studies of nox on well-mixed oxides derived from co-mg/al hydrotalcite-like compounds. *The journal of physical chemistry. B*, 110(9), March 2006.
- [61] Eli Ruckenstein Yun Hang Hu. Binary mgo-based solid solution catalysts for methane conversion to syngas. *Catalysis Reviews*, 44:3, 423-453, DOI: 10.1081/CR-120005742, 2002.
- [62] M. Zanfiri and A. Gavrilidis. Catalytic combustion assisted methane steam reforming in a catalytic plate reactor. *Chemical Engineering Science*, 58(17):3947–3960, 2003.
- [63] U Zavyalova, P Scholz, and B Ondruschka. Influence of cobalt precursor and fuels on the performance of combustion synthesized  $\text{Co}_3\text{O}_4/\gamma\text{-Al}_2\text{O}_3$  catalysts for total oxidation of methane. *Applied Catalysis A: General*, 323:226–233, April 2007.
- [64] Jianguo Zhang, Hui Wang, and Ajay K. Dalai. Effects of metal content on activity and stability of ni-co bimetallic catalysts for  $\text{CO}_2$  reforming of  $\text{CH}_4$ . *Applied Catalysis A, General*, 339(2):121–129, 2008.
- [65] Jianqiang Zhu, Xiaoxi Peng, Lu Yao, Jing Shen, Dongmei Tong, and Changwei Hu. The promoting effect of la, mg, co and zn on the activity and stability of ni/sio<sub>2</sub> catalyst for  $\text{CO}_2$  reforming of methane. *International Journal of Hydrogen Energy*, 36(12):7094–7104, 2011.
- [66] Marcus F. M. Zwinkels, Sven G. Jrs, P. Govind Menon, and Timothy A. Griffin. Catalytic materials for high-temperature combustion. *Catalysis Reviews*, 35(3):319–358, August 1993.

# Calculation

## A.1 Calculations for the preparation of the catalysts

### A.1.1 Calculations for the hydrotalcite catalyst preparations

The goal of these calculations is to get the general formula of hydrotalcites:



see chapter 2.1 for more explanations.

The composition calculations of  $Ni - Co/MgO/Al_2O_3$  starts as following:

$$\frac{z}{q + x + y + z} = \frac{1}{4} \quad (\text{A.2})$$

where

q = moles  $Co^{2+}$

x = moles  $Ni^{2+}$

y = moles  $MgO$

z = moles  $Al_2O_3$

For one mole  $Al^{3+}$ , z=1, so that Equation A.2 becomes as following:

$$q + x + y = 3 \Rightarrow y = 3 - q - x \quad (\text{A.3})$$

---

The weight fractions of Co ( $w_{Co}$ ) and Ni ( $w_{Ni}$ ) are defined:

$$w_{Co} = \frac{m_{Co}}{m_{Co} + m_{Ni} + m_{MgO} + m_{Al_2O_3}} \quad (A.4)$$

$$w_{Ni} = \frac{m_{Ni}}{m_{Ni} + m_{Co} + m_{MgO} + m_{Al_2O_3}} \quad (A.5)$$

Let these definitions hold:

$m_i$  = weight/mass of component i

$M_i$  = molar mass of component i

$n_i$  = number moles of component i

By using relations  $m_i = n_i \cdot M_i$ ,  $n_i = [q, x, y, z] \Rightarrow$  Equation A.4 and Equation A.5 become:

$$w_{Co} = \frac{q \cdot M_{Co}}{q \cdot M_{Co} + x \cdot M_{Ni} + y \cdot M_{MgO} + M_{Al_2O_3}} \quad (A.6)$$

$$w_{Ni} = \frac{x \cdot M_{Ni}}{q \cdot M_{Co} + x \cdot M_{Ni} + y \cdot M_{MgO} + M_{Al_2O_3}} \quad (A.7)$$

Putting Equation A.3 into equation Equation A.7, the following relation is obtained:

$$x = \frac{w_{Ni}(q \cdot M_{Co} + q \cdot M_{MgO} + 3M_{MgO} + 0.5M_{Al_2O_3})}{M_{Ni}(1 - w_{Ni}) + w_{Ni}M_{MgO}} \quad (A.8)$$

Moles of Co is obtained by inserting Equation A.3 and Equation A.8 in Equation A.6:

$$q = \frac{3M_{MgO} + 0.5M_{Al_2O_3}}{\frac{M_{Co}}{w_{Co}}((1 - w_{Ni}) + w_{Ni} \cdot \frac{M_{MgO}}{M_{Ni}}) - M_{Co} + M_{MgO}} \quad (A.9)$$

Using different weight fractions of nickel and cobalt, their moles are given in Table A.1.

**Table A.1:** The estimation of mole numbers of different components derived from hydrotalcite precursors.

Metal Loading [%]		Mass fraction [-]		q	x	y	z
Ni	Co	$w_{Ni}$	$w_{Co}$				
12	0	0.12	0	0	0.37	2.63	1
0	12	0	0.12	0.36	0	2.64	1
3.6	8.4	0.036	0.084	0.25	0.11	2.64	1

Since there are two moles  $Al^{3+}$  in  $Al_2O_3$ , [Table A.1](#) must be doubled to get correct mole numbers of every component in the HT-precursors. This is given in [Table A.2](#).

**Table A.2:** The stoichiometric coefficients of atomic ions forming hydrotalcite precursors.

Catalyst	Stoichiometric coefficients					
	$Ni^{2+}$	$Co^{2+}$	$Mg^{2+}$	$Al^{3+}$	$OH^-$	$CO_3^{2-}$
12 % Ni	0.74	0	5.26	2	16	1
12 % Co	0	0.72	5.28	2	16	1
3.6 %Ni-8.4 % Co	0.22	0.5	5.28	2	16	1

[Table A.3](#) is obtained by putting values from [Table A.2](#) into [Equation A.1](#) and it is showing the general hydrotalcite formulas for the prepared catalysts.

**Table A.3:** Hydrotalcite formulas of different catalysts.

Catalyst	Formula
12 % Ni	$[Ni_{0.74}^{2+}Mg_{5.26}^{2+}Al_2^{3+}(OH)_{16}^-]^{2+}CO_3^{2-}.mH_2O$
12 % Co	$[Co_{0.72}^{2+}Mg_{5.28}^{2+}Al_2^{3+}(OH)_{16}^-]^{2+}CO_3^{2-}.mH_2O$
3.6 % Ni-8.4 % Co	$[Ni_{0.22}^{2+}Co_{0.5}^{2+}Mg_{5.28}^{2+}Al_2^{3+}(OH)_{16}^-]^{2+}CO_3^{2-}.mH_2O$

[Table A.4](#) gives an overview of the nominal mass of precursors of different metal loading, while the actual mass used in this thesis is given in [Table A.5](#).

**Table A.4:** Nominal mass of precursors of different metal loading.

Catalyst	Mass of reactant [g]					
	$Ni(NO_3)_2 \cdot 6H_2O$	$Co(NO_3)_2 \cdot 6H_2O$	$Mg(NO_3)_2 \cdot 6H_2O$	$Al(NO_3)_3 \cdot 9H_2O$	NaOH	$Na_2CO_3$
12% Ni	7.96	0	50.67	28.13	24.00	5.96
12% Co	0	7.94	50.67	28.13	24.00	5.96
3.6%Ni- 8.4%Co	02.39	5.56	50.69	28.13	24.00	5.96

**Table A.5:** Mass of precursors of different metal loading used in this project.

Catalyst	Mass of reactant [g]					
	$Ni(NO_3)_2 \cdot 6H_2O$	$Co(NO_3)_2 \cdot 6H_2O$	$Mg(NO_3)_2 \cdot 6H_2O$	$Al(NO_3)_3 \cdot 9H_2O$	NaOH	$Na_2CO_3$
12% Ni	7.9732	0	50.7806	28.1570	24.0588	5.9687
12% Co	0	7.94866	50.7072	28.0763	24.0462	5.6904
3.6%Ni- 8.4%Co	2.3948	5.5615	50.7072	28.1795	24.0551	5.9674

## A.1.2 Calculations for the promoted catalyst

To promote the catalysts with lanthanum, incipient impregnation wetness method was used. First salt from lanthanum(III)-nitrate-hydrate was well mixed with small amounts of distilled water. Then the solution was added to the reduced and passivated catalyst.

The amount of lanthanum (La) in the precursor ( Lanthanum(III)-nitrate-hydrate) was determined by TGA-analysis, which showed that there is 0.3155 g La/ 1 g Lanthanum(III)-nitratehydrate salt. Based on this relation, 0.3155 g La/ 1 g salt, the needed salt for every catalyst was calculated and is shown in [Table A.6](#)

**Table A.6:** Calculated amounts for the promoted catalysts.

Catalyst mass [g]	Promoted lanthanum (La) [g]	Mass of Lanthanum(III)-nitratehydrate [g]
0.995	0.005	0.015848294
0.999	0.01	0.031696588
0.980	0.02	0.063393175

The up-taken amount of water was found from the pore volume with the below relation:

$$V_{water} = V_P$$

, where  $V_{water}$  is the up-taken amount of water and  $V_P$  is the pore volume of the catalyst which is determined by the BET analysis. The values of  $V_{water}$  are presented in [Table A.7](#).

---

To get the correct amount of water, the mass of the catalyst must be multiplied to the  $V_{water}$ -values.

**Table A.7:** Amount of water for the different catalysts.

Catalyst	$V_{water}$ [ $cm^3/g$ ]
12Ni	0.397301
12Co	0.536223
3.6Ni-8.4Co	0.458796

## A.2 Catalytic activity calculations

### A.2.1 Derivation of the methane conversion

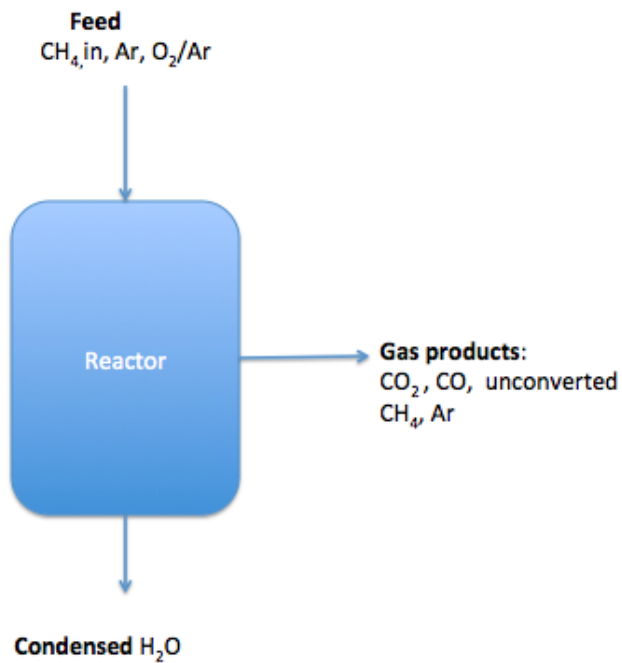


**Figure A.1:** Mass flow principle sketch.

The out stream from the reactor are  $CO_2$ ,  $CH_4$ ,  $CO$ ,  $H_2O$  and  $Ar$ , where  $CO_2$  and  $H_2O$  are desired reaction products,  $CH_4$  is unconverted methane,  $CO$  is the undesired product and  $Ar$  is an inert gas, see figure [Figure A.1](#). Water,  $H_2O$  does not enter the GC,

---

since it is condensed. The amount of methane converted to other components,  $X_{CH_4}$  is defined as:

$$X_{CH_4} = \frac{F_{CH_4,in} - F_{CH_4,out}}{F_{CH_4,in}} \quad (A.10)$$

The numerator is the converted methane products, namely:

$$X_{CH_4} = \frac{F_{CO_2,out} + F_{CO,out}}{F_{CH_4,in}} \quad (A.11)$$

$F_{CH_4,in}$  goes also out as  $F_{CO_2,out}$ ,  $F_{CO,out}$  and  $F_{CH_4,out}$ , so [Equation A.11](#) becomes:

$$X_{CH_4} = \frac{F_{CO_2,out} + F_{CO,out}}{F_{CO_2,out} + F_{CO,out} + F_{CH_4,out}} \quad (A.12)$$

The flow rate of the components is product of the total flow rate,  $F_{tot}$  and component's concentration.

$$X_{CH_4} = \frac{F_{tot}(C_{CO_2,out} + C_{CO,out})}{F_{tot}(C_{CO_2,out} + C_{CO,out} + C_{CH_4,out})} \quad (A.13)$$

So the final equation is

$$X_{CH_4} = \frac{C_{CO_2,out} + C_{CO,out}}{C_{CO_2,out} + C_{CO,out} + C_{CH_4,out}} \quad (A.14)$$

, where the concentrations are calculated from the GC-data, using the response factors given in [table Table A.8](#).

**Table A.8:** The response factor for  $i$  molecules,  $R_i$ .

Molecule	$R_i$
$CH_4$	0.02984
$CO_2$	0.027532
$CO$	0.02288

## A.2.2 Normalization of the UV-Vis data

When the normalization of the UV-Vis spectra data was calculated, the following equation is used:

$$f = \frac{R_i - R_{min}}{R_{max} - R_{min}} \quad (A.15)$$

, where is  $R$  is the reflectance value.  $f$  : The oxidation state fraction

$R_i$  : Reflectance of oxidation state at different temperatures  $\implies R_i(\text{Ox}, T)$ , is function of oxidation state (Ox) and temperature (T)



$R_{min}$  : reflectance of Oxidation state where the catalyst is 100 % reduced at cooling temperature  $\implies R_{min}(Ox,T)$

$R_{max}$  : Reflectance of maximum oxidation state referring to when the catalyst is 100 % oxidized  $\implies R_{max}(Ox,T)$

Table A.9 is showing the reflectance values for both  $R_{max}$  and  $R_{min}$ , meaning the oxidation state reflectance values lie in this region.

**Table A.9:** The reflectance for maximum and minimum oxidation states at wavelength of 540 nm for 12Ni.

Unit	Reflectance
$R_{max}$	75.45719
$R_{min}$	31.77173

When the reflectance obtained from the cooling down reduction conditions were plotted against the cooling temperature, the following equation was found:

$$Reflectance = -0.005x + 34.483$$

where  $-0.005$  is the slope, denoted by  $y$  in below equations.

$$R_{max}(Ox, T) = R_{max} - y(T - T_{max}) \quad (A.16)$$

$$R_{min}(Ox, T) = R_{min} + y(T - T_{min}) \quad (A.17)$$

, where  $R_{max}$  and  $R_{min}$  are given in Table A.9,  $T_{max}$  is the temperature which gives the highest oxidation state ( $R_{max}$ ) and  $T_{min}$  is the temperature which gives the lowest oxidation state ( $R_{min}$ ) at wavelength of 540 nm.

Obtaining  $R_{in}$  from the reflectance at different temperatures during the methane combustion, the oxidation state fraction was calculated from Equation A.15 and  $f$  was plotted against  $T$ , revealing how the oxidation fraction is only function of the temperature at 540 nm.

## A.3 Other calculations

### A.3.1 Calculation of the error of the BET instrument

To determine the instrumental error from the BET analyzes, 12Co-2La was analyzed three time and the following method based on the standard deviation was used, Table A.10:

**Table A.10:** Sample variance, average and pore diameter of the catalysts.

Sample variance of 12Co-2La (x) [ $m^2/g$ ]	Average (A) [ $m^2/g$ ]	$(x - A)^2 [(m^2/g)^2]$
118	119	1
118		1
121		4

The mean of the squared values is  $((1+1+4)/3 = 2)$  2 and by taking the square root of 2 the deviation is 1.4.

### A.3.2 Calculation of the covered/blocked amount by lanthanum (La)

The fraction of covered/blocked amounts by lanthanum is calculated as following: If you have 100 g catalyst, 12 % of it is nickel(Ni)  $\implies$  there is 12 g nickel. The dispersion of nickel is 7.4 % obtained from the chemisorption data. Then there is  $12 \text{ g} * 7.4 \% = 0.888 \text{ g Ni}/(58.7 \text{ g/mole}) = 0.0151 \text{ mole Ni}$ .

In 12Ni-2La catalyst there is 1.32 % lanthanum (La) as confirmed by the ICP-MS analyzes. The number of moles of La:

$1.32 \text{ g La}/138.91 \text{ g/mole} = 9.5 * 10^{-3} \text{ mole}$ , where 37 % of it is on the surface, obtained from the ratio between metallic surface area and BET surface area of Ni ( $\frac{50m^2/g}{135m^2/g} = 0.37$ )  $\implies$  there is  $3.52 * 10^{-3} \text{ mole La}$  covering the active sites of Ni whereby 23.3 % of Ni is covered/blocked by La:

$$\frac{0.0151 \text{ mole}}{3.52 * 10^{-3} \text{ mole}} = 0.233$$

# Appendix **B**

## Aspects of the catalysts

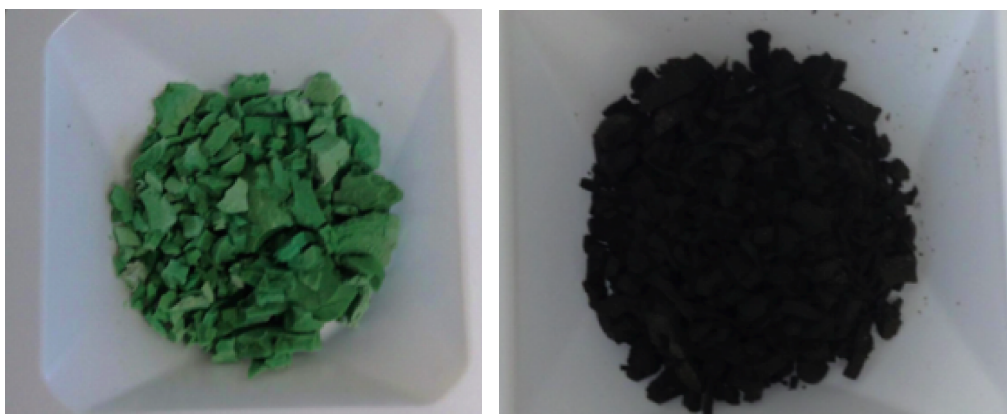


**Figure B.1:** The prepared and calcined catalysts. Left: 12 *wt.* % Ni, right: 12 *wt.* % Co.

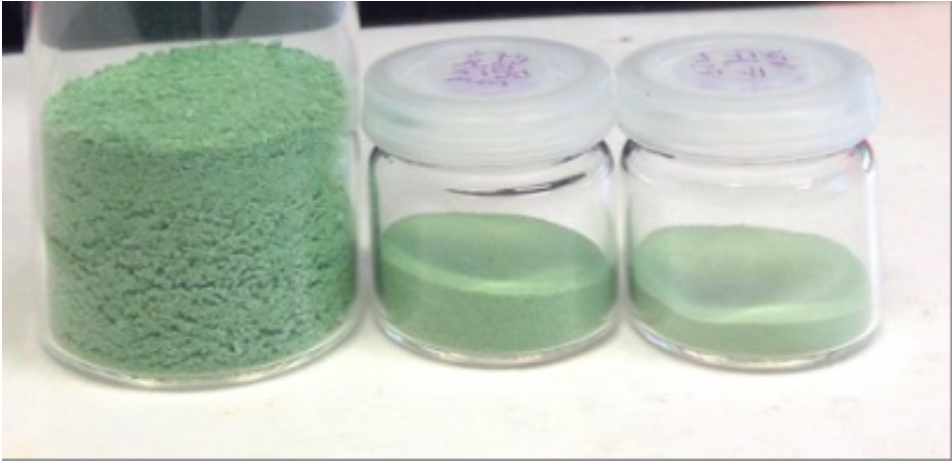


**Figure B.2:** 12 wt. % Ni in different sizes after calcination step. From left to right: size  $\geq 150 \mu m$ ,  $75 \mu m \leq \text{size} \leq 150 \mu m$  and size  $\leq 75 \mu m$ .

# Appendix C

## Appendix of figures

Figure C.1–Figure C.9 present the adsorption-desorption isotherms from the BET analyzes. Figure C.10–Figure C.12 present the Langmuir isotherms from hydrogen chemisorption, while Figure C.13–C.14 are showing the results from MS during methane combustion.

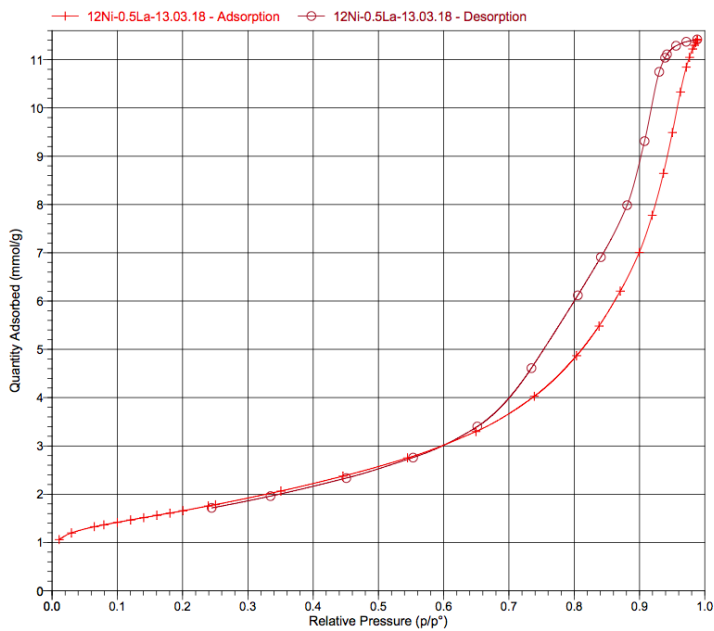
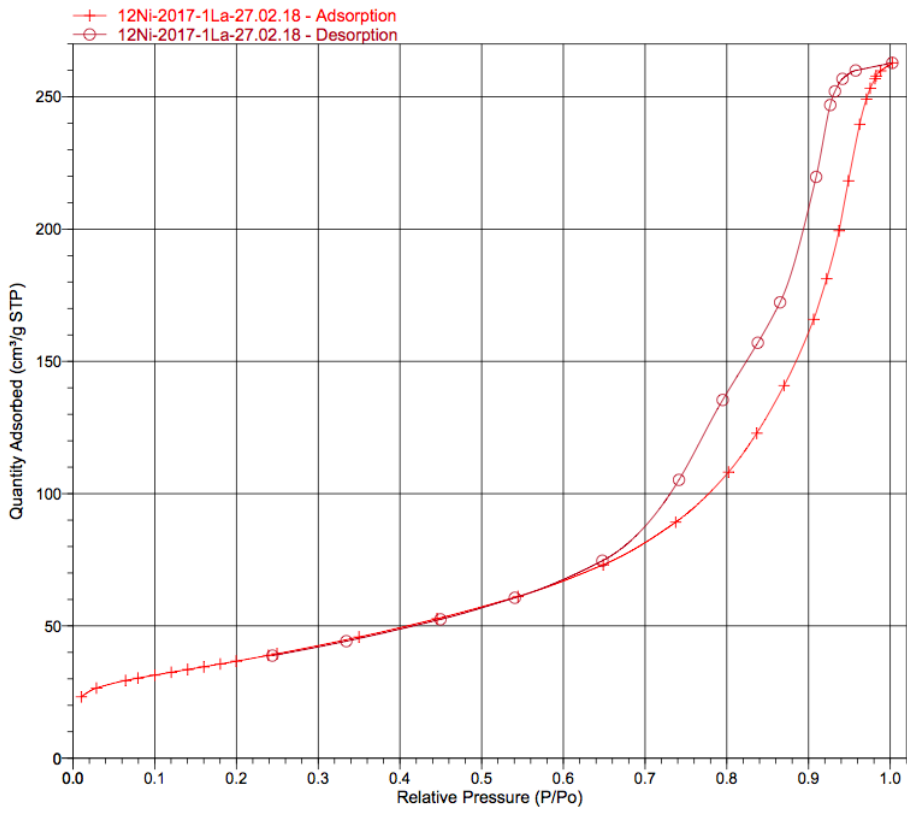
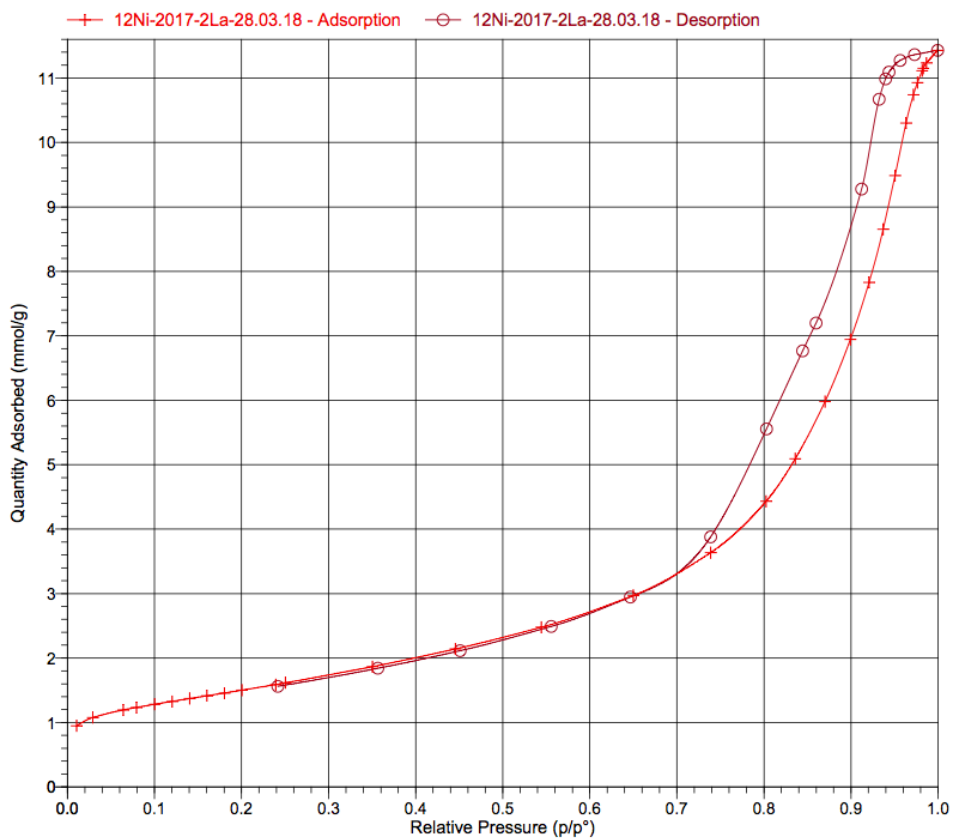


Figure C.1: Isotherm linear plot for 12Ni-0.5La.



**Figure C.2:** Isotherm linear plot for 12Ni-1La.



**Figure C.3:** Isotherm linear plot for 12Ni-2La.

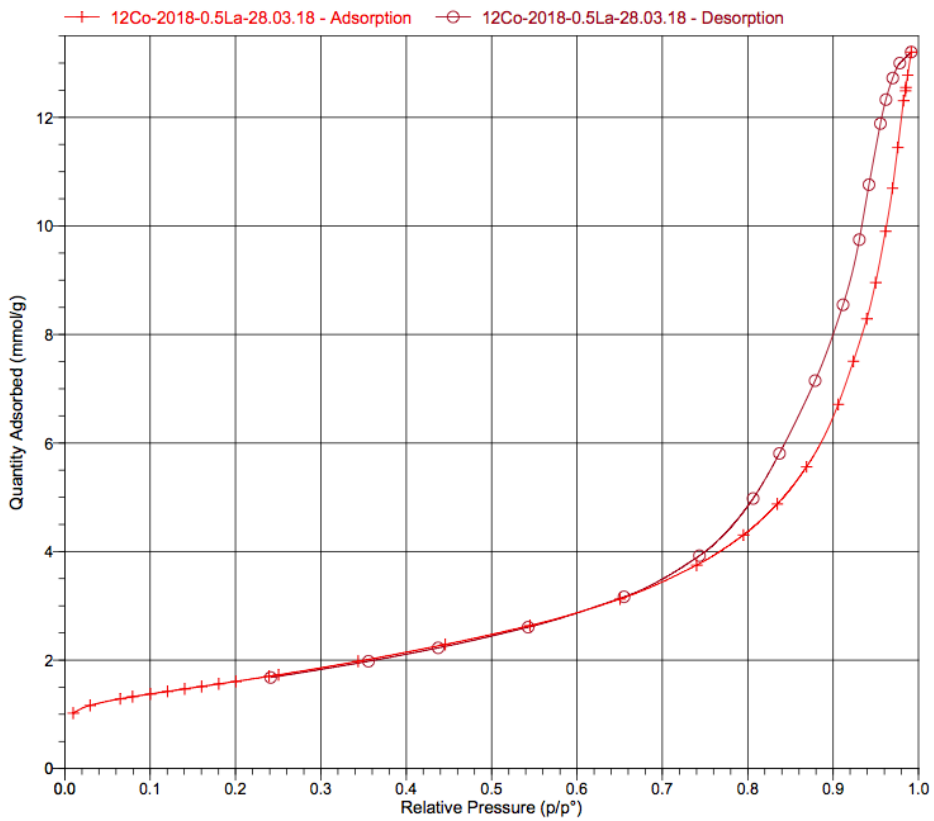
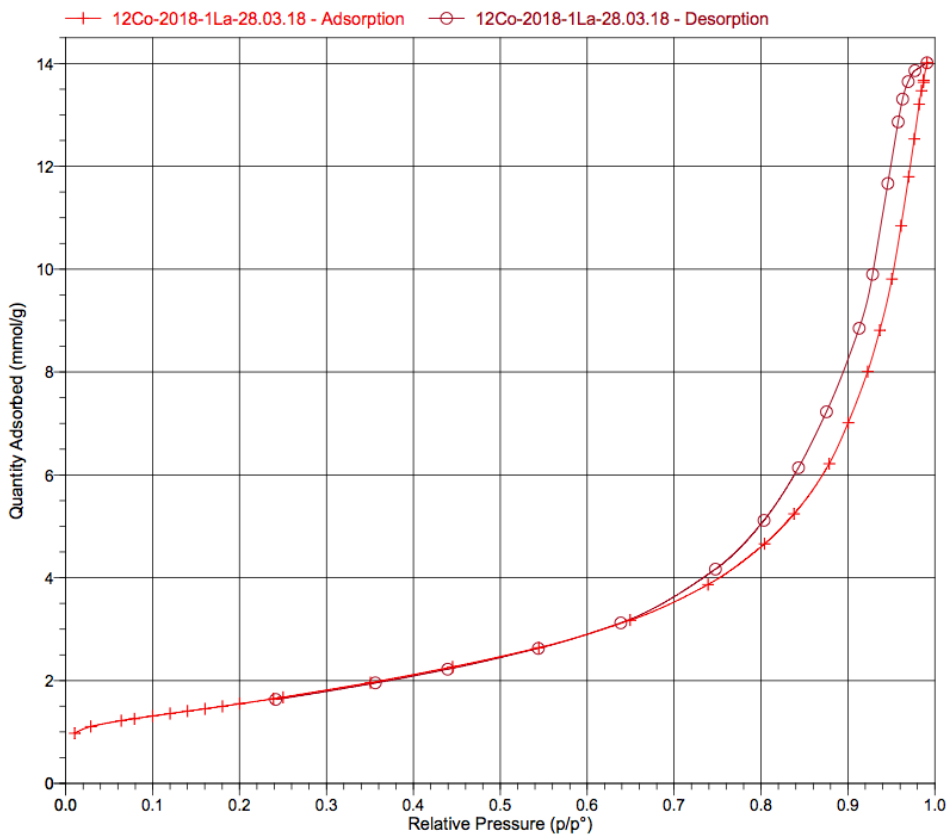


Figure C.4: Isotherm linear plot for 12Co-0.5La.





**Figure C.5:** Isotherm linear plot for 12Co-1La.

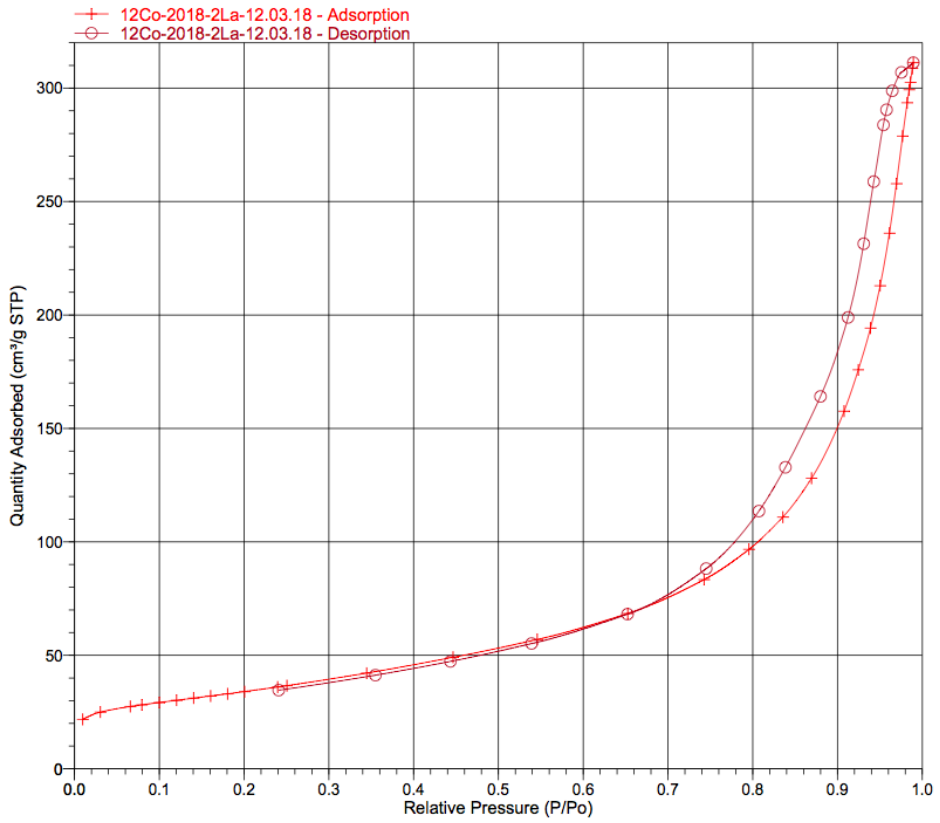
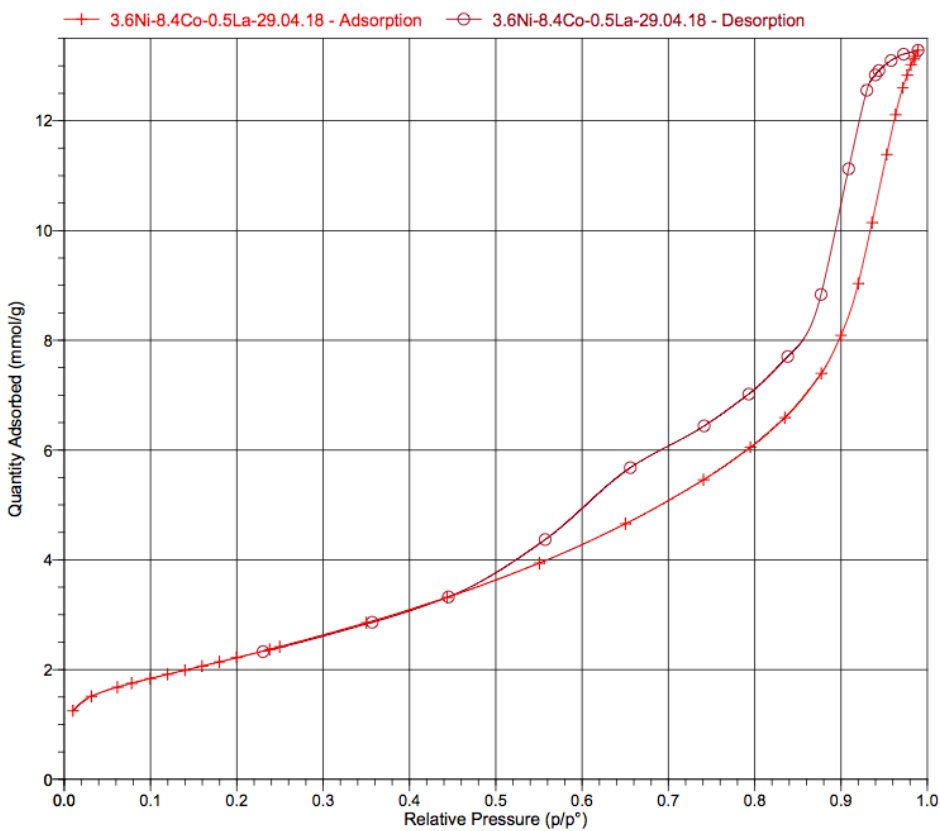
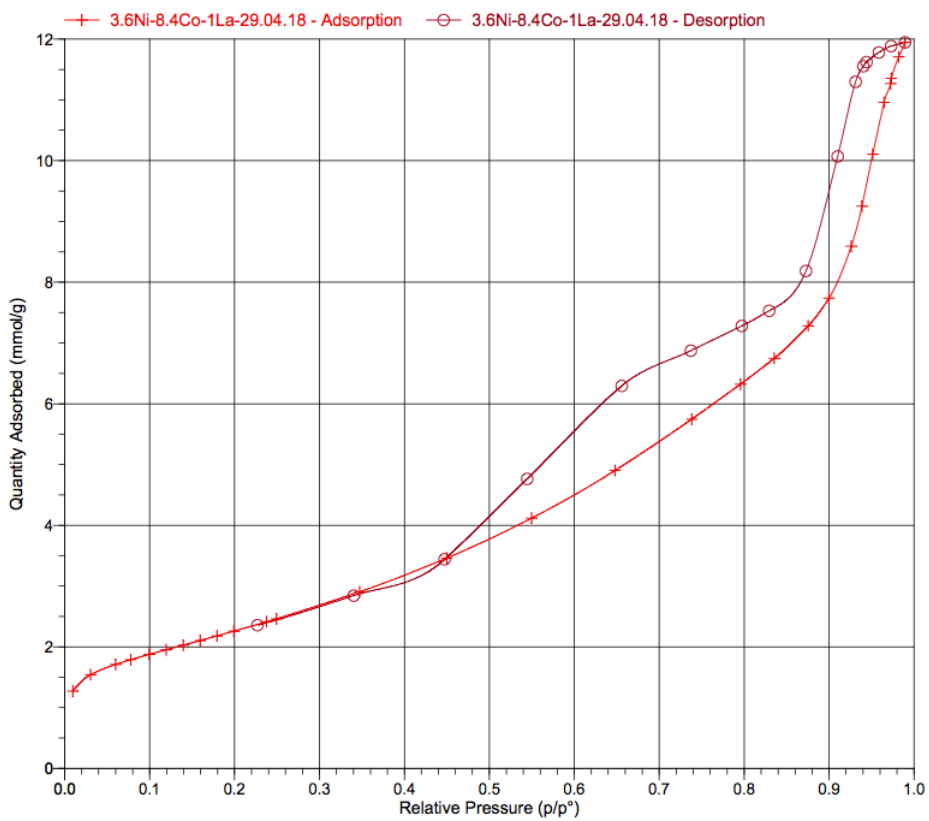


Figure C.6: Isotherm linear plot for 12Co-2La.



**Figure C.7:** Isotherm linear plot for 3.6Ni-8.4Co-0.5La.



**Figure C.8:** Isotherm linear plot for 3.6Ni-8.4Co-1La.

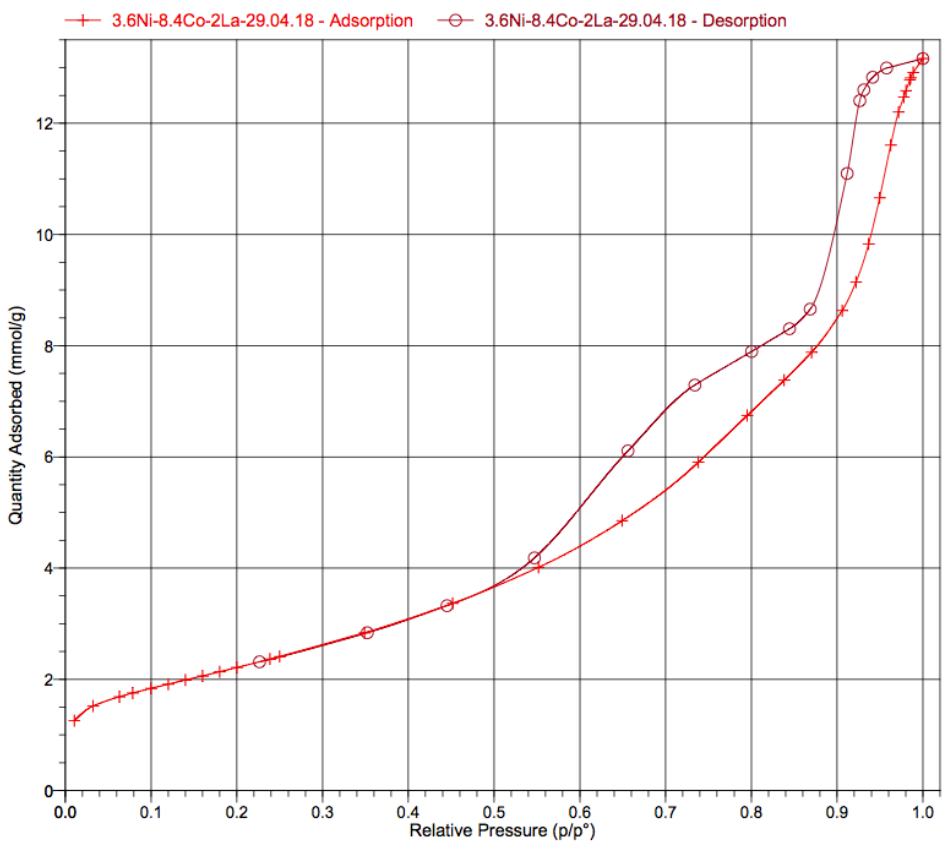


**Figure C.9:** Isotherm linear plot for 3.6Ni-8.4Co-2La.

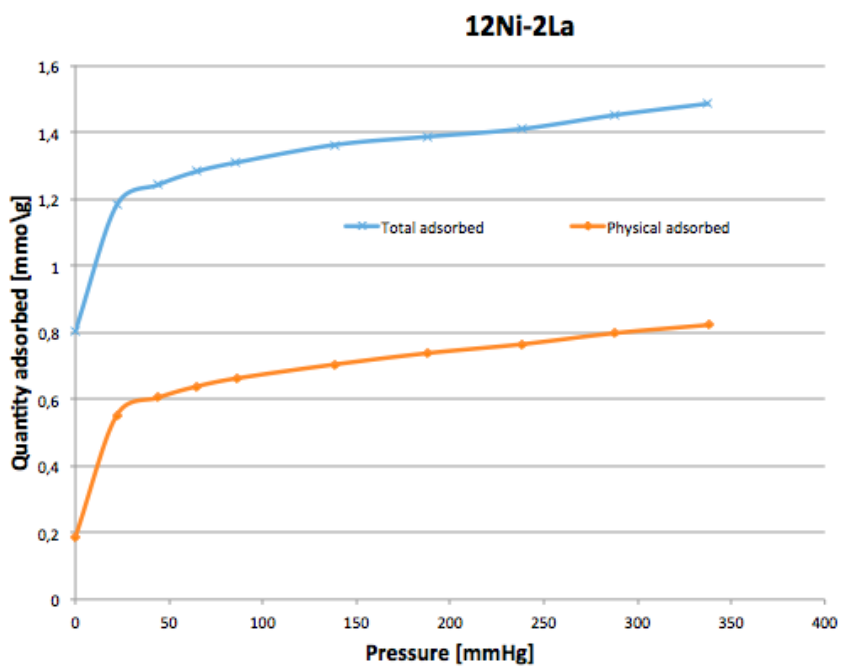
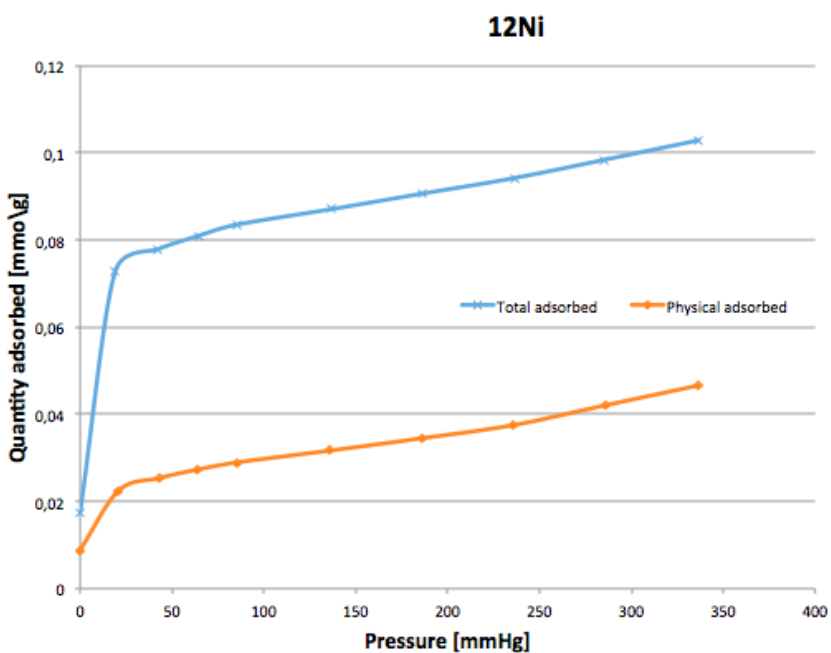


Figure C.10: Hydrogen chemisorption isotherms for 12Ni and 12Ni-2La.

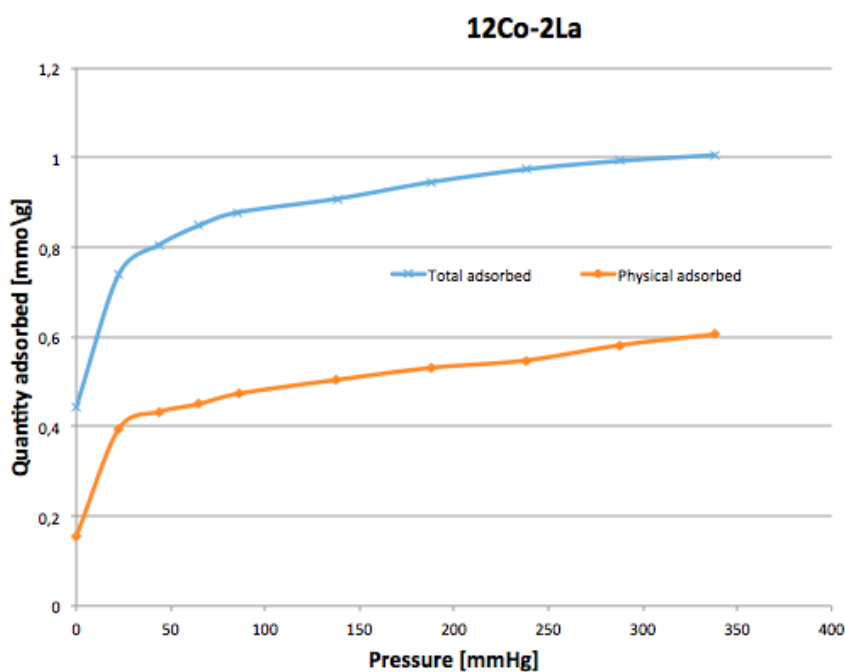
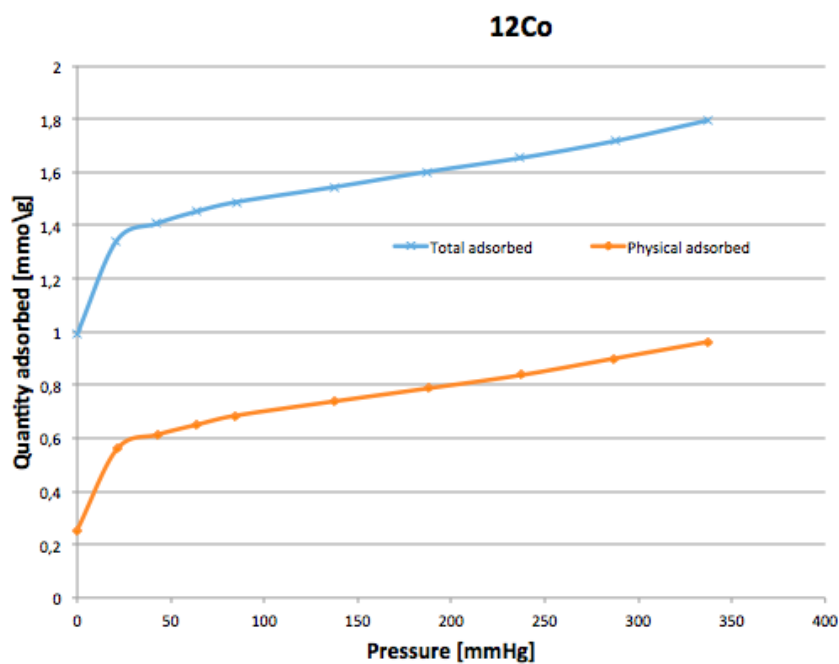


Figure C.11: Hydrogen chemisorption isotherms for 12Co and 12Co-2La.

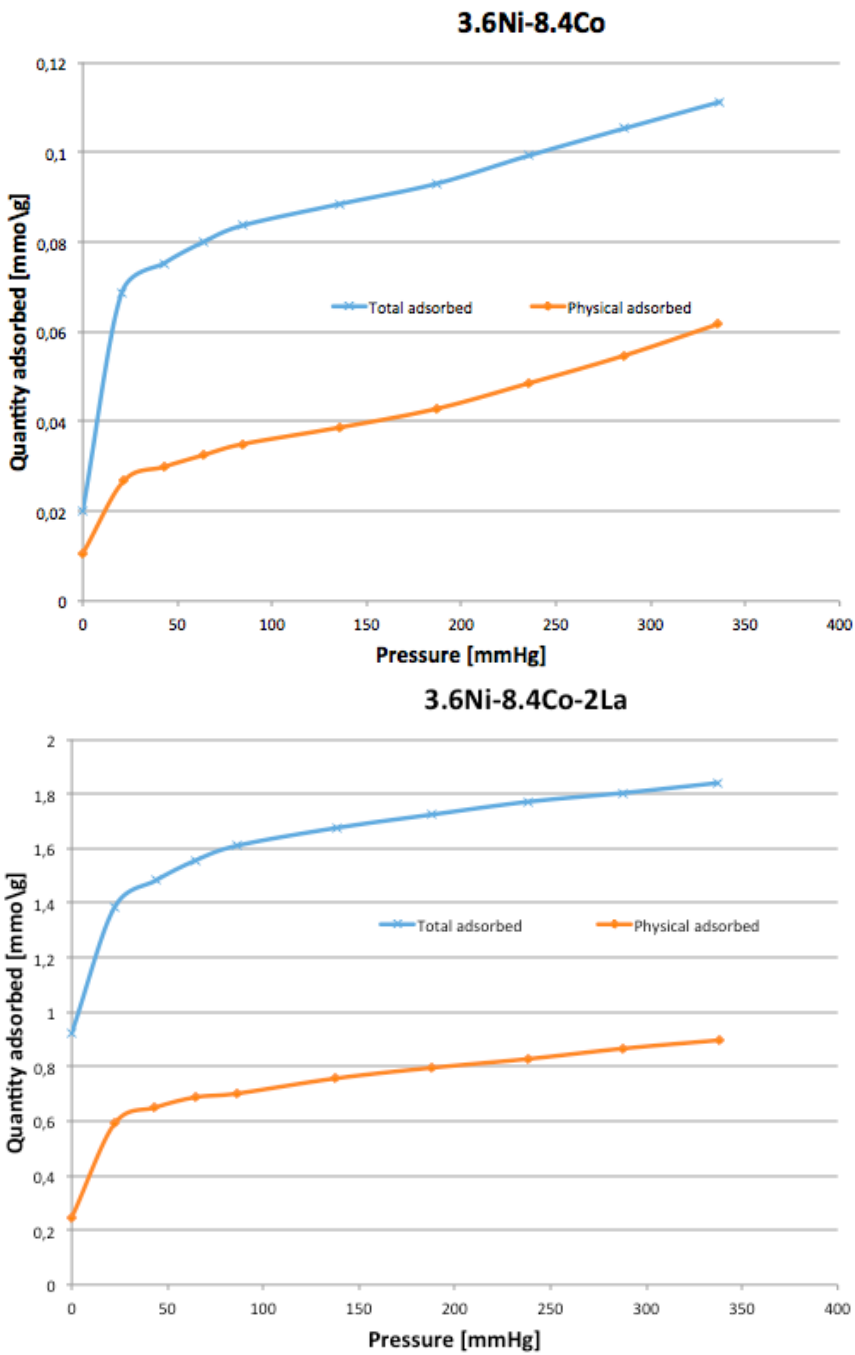
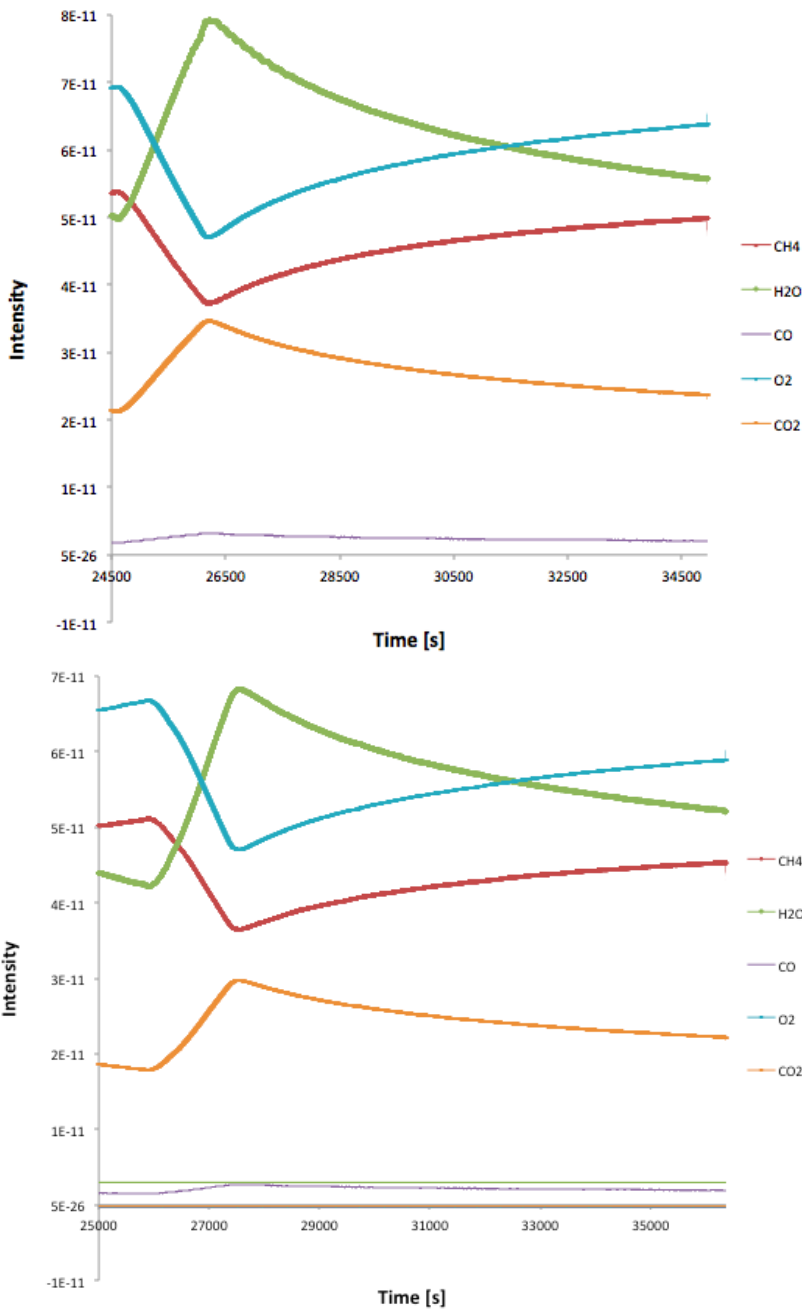
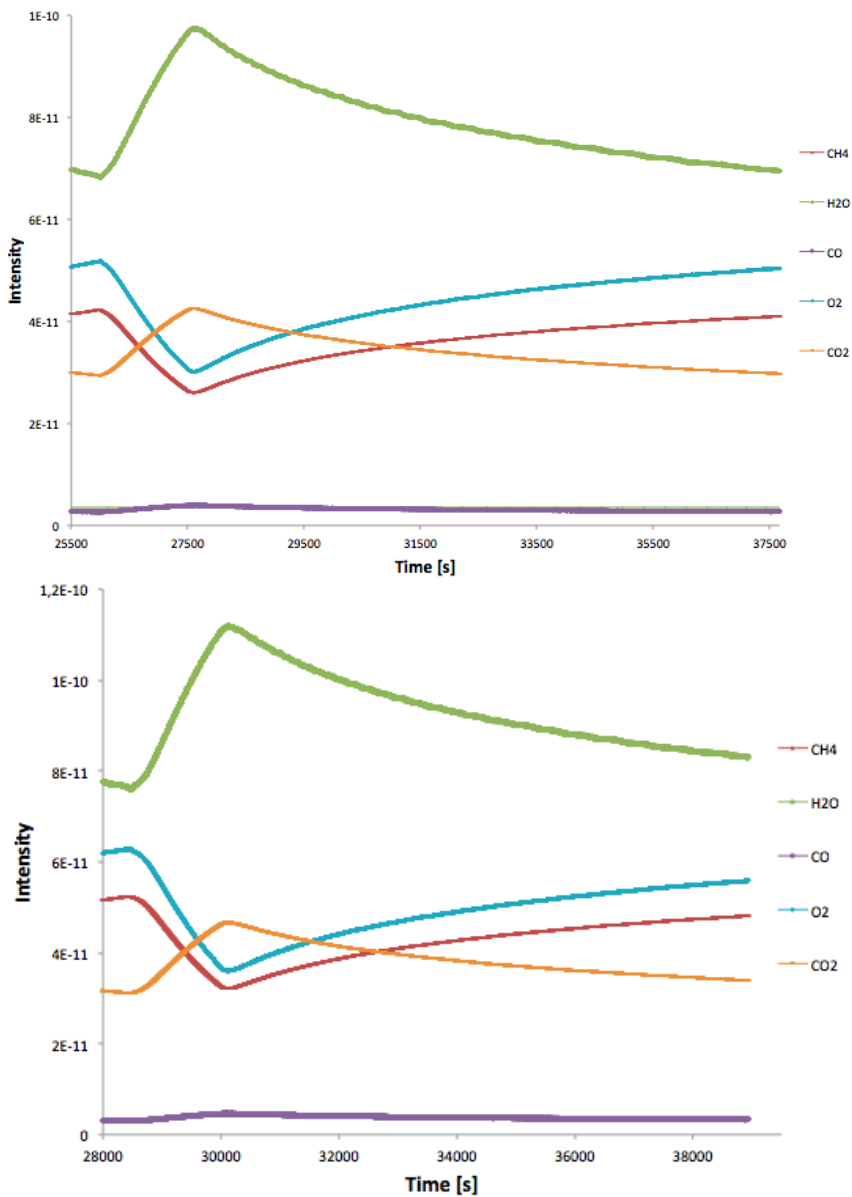


Figure C.12: Hydrogen chemisorption isotherms for 3.6Ni-8.4Co and 3.6Ni-8.4Co-2La.





**Figure C.13:** The MS-intensity as function of time during the isothermal (500 °C) combustion of methane. Reaction conditions: 0.5 g catalyst diluted with 2 g  $\alpha$ - $Al_2O_3$ , 1.5 mL/min  $CH_4$ , 7.5 mL/min 50 %  $O_2$ /Ar and 142 mL/min Ar. Top: 12Co, bottom: 12Co-2La.



**Figure C.14:** The MS-intensity as function of time during the isotherm (500 °C) combustion of methane. Reaction conditions: 0.5 g catalyst diluted with 2 g  $\alpha\text{-Al}_2\text{O}_3$ , 1.5 mL/min  $\text{CH}_4$ , 7.5 mL/min  $\text{O}_2/\text{Ar}$  and 142 mL/min  $\text{Ar}$ . Top: 3.6Ni-8.4Co, bottom: 3.6Ni-8.4Co-2La.

# Appendix D

## Appendix of files

The below forms are showing the correction files for the TGA conditions.

<b>Instrument:</b>	NETZSCH STA 449 C	<b>Sample Mass:</b>	33.000 mg
<b>Project:</b>	Master	<b>Reference Name:</b>	cal
<b>Filename:</b>	Lanthanumnitrate240118.dsu	<b>Reference Mass:</b>	0.000 mg
<b>Sample Identity:</b>	Lanthanumnitrate240118	<b>Reference Crucible Mass:</b>	0.000 mg
<b>Date/Time:</b>	24.01.2018 08:57:07	<b>Sample Material:</b>	blank
<b>Laboratory:</b>	Najma	<b>Correction Filename:</b>	Correction_Lanthanumnitrate.bsu
<b>Operator:</b>	Najma	<b>Temp.Calib. Filename:</b>	021017_Ar_80ml.tsu
<b>Measurement Mode:</b>	DSC-TG	<b>Sensitivity Filename:</b>	021017_Ar_80ml.esu
<b>Type of measurement:</b>	Sample + Correction	<b>Crucible Name:</b>	DSC/TG pan Al2O3
<b>Sample Name:</b>	Correction_Lanthanumnitrate		

**Remark:**

<b>Furnace:</b>	STD Sic 2	<b>Equil. Threshold:</b>	5.0 K
<b>Sample Carrier:</b>	DSC/(TG) HIGH RG 4	<b>Measurement End:</b>	Normal end
<b>M.range (DSC):</b>	5000 $\mu$ V	<b>Furnace TC:</b>	S
<b>M.range (TG):</b>	5000 mg	<b>Sample TC:</b>	S
<b>Pre.Heating Threshold:</b>	15.0 K	<b>Crucible Mass:</b>	148.200 mg

<b>Purge 1 MFC:</b>	AIR(80/20)	<b>Flow range:</b>	249.5 ml/min
<b>Purge 2 MFC:</b>	CARBON DIOXIDE	<b>Flow range:</b>	175.0 ml/min
<b>Protective MFC:</b>	ARGON	<b>Flow range:</b>	312.5 ml/min

List of temperature steps:

Num	Mode	Temp. °C	HR K/min	Acq.Rate pts/min	Duration hh:mm	STC	P1:N2/O2	P2:--	PG:Ar
---	Start	30.0				1	75.0	0.0	25.0
1	Dynamic	900.0	5.00	75.00	02:54	1	75.0	0.0	25.0
2	Isothermal	900.0		1.39	03:00	1	75.0	0.0	25.0
---	Emergency	920.0					75.0	0.0	25.0

**Figure D.1:** TGA conditions; Lanthanum nitrate hydrate was heated 5 °C/min from 30 °C to 900 °C with 75 mL/min air and 25 mL/min Ar (inert gas) and isotherm treatment at 900 °C for 3 h.

<b>Instrument:</b>	NETZSCH STA 449 C	<b>Sample Name:</b>	Najma
<b>Project:</b>		<b>Sample Mass:</b>	0.000 mg
<b>Filename:</b>	Correctionfile_C-Formation_040618.bsu	<b>Reference Name:</b>	cal
<b>Sample Identity:</b>	Correctionfile_Co_040618	<b>Reference Mass:</b>	0.000 mg
<b>Date/Time:</b>	04.06.2018 09:36:50	<b>Reference Crucible Mass:</b>	0.000 mg
<b>Laboratory:</b>		<b>Sample Material:</b>	blank
<b>Operator:</b>	KarolineNielsen	<b>Temp.Calib. Filename:</b>	021017_Ar_80ml.tsu
<b>Measurement Mode:</b>	DSC-TG	<b>Sensitivity Filename:</b>	021017_Ar_80ml.esu
<b>Type of measurement:</b>	Correction	<b>Crucible Name:</b>	DSC/TG pan Al2O3

**Remark:**

<b>Furnace:</b>	STD SiC 2	<b>Equil. Threshold:</b>	5.0 K
<b>Sample Carrier:</b>	DSC/(TG) HIGH RG 4	<b>Measurement End:</b>	Normal end
<b>M.range (DSC):</b>	5000 $\mu$ V	<b>Furnace TC:</b>	S
<b>M.range (TG):</b>	5000 mg	<b>Sample TC:</b>	S
<b>Pre.Heating Threshold:</b>	15.0 K	<b>Crucible Mass:</b>	148.000 mg

**Purge 1 MFC:** AIR(80/20)      **Flow range:** 249.5 ml/min  
**Purge 2 MFC:** CARBON DIOXIDE      **Flow range:** 175.0 ml/min  
**Protective MFC:** ARGON      **Flow range:** 312.5 ml/min

List of temperature steps:

Num	Mode	Temp. °C	HR K/min	Acq.Rate pts/min	Duration hh:mm	STC	P1:N2/O2	P2:--	PG:Ar
---	Start	31.0				1	0.0	0.0	25.0
1	Dynamic	120.0	10.00	100.00	00:08	1	0.0	0.0	25.0
2	Isothermal	120.0		4.18	01:00	1	0.0	0.0	25.0
3	Dynamic	31.0	10.00	100.00	00:08	1	0.0	0.0	25.0
4	Isothermal	31.0		8.33	00:30	1	0.0	0.0	25.0
5	Dynamic	900.0	10.00	100.00	01:26	1	75.0	0.0	25.0
6	Isothermal	900.0		1.39	03:00	1	75.0	0.0	25.0
---	Emergency	920.0					75.0	0.0	25.0

**Figure D.2:** TGA conditions; The spent catalysts were heated 10 °C/min from 31 °C to 900 °C with 75 mL/min air and 25 mL/min Ar (inert gas) and isotherm treatment at 900 °C for 3 h.